Int J Earth Sci (Geol Rundsch) (2006) 95: 504–528
DOI 10.1007/s00531-005-0027-9

ORIGINAL PAPER

A. C. Adriasola · S. N. Thomson · M. R. Brix
F. Hervé · B. Stöckhert

Postmagmatic cooling and late Cenozoic denudation of the North Patagonian Batholith in the Los Lagos region of Chile, 41°–42°15′S

Received: 7 October 2004 / Accepted: 18 June 2005 / Published online: 8 October 2005

Abstract Zircon and apatite fission track (FT) thermochronology was applied to investigate the history of cooling and denudation of the Southern Andes between 41° and 42°15′S in relation to the late Cenozoic activity of the Liquiñe-Ofqui fault zone (LOFZ) and the northward migration of the Chile Triple Junction (CTJ). Fifty-six zircon and 51 apatite FT ages, plus 37 apatite confined track-length distributions were obtained mainly from plutonic rocks of the North Patagonian Batholith (NPB) in the main Andean Cordillera. Apatite FT ages and track lengths indicate a stage of rapid cooling at ~5–3 Ma along both sides of the LOFZ, whereas older Miocene ages with monotonous cooling histories were obtained further away from the fault. Zircon FT ages range from Cretaceous to Pliocene, with marked differences observed along and across the LOFZ. Three different types of temperature-time histories characterise the post-magmatic cooling of the NPB in the region: deep intrusions with moderate and steady cooling rates, intrusions in the upper crust with very slow cooling rates following a stage of initial rapid cooling, and rapidly cooled and exhumed shallow intrusions, the latter with younger ages towards the fault zone. The most prominent denudation episode along the LOFZ is late Miocene to Pliocene, coeval with plate tectonic reconstructions for the arrival and subduction of the Chile Rise beneath the Taitao Peninsula.

A. C. Adriasola (✉) · M. R. Brix · B. Stöckhert
Institut für Geologie, Mineralogie und Geophysik,
Ruhr-Universität Bochum, 44780 Bochum, Germany
E-mail: alberto.adriasola@gmx.de

S. N. Thomson
Department of Geology and Geophysics, Yale University,
P.O. Box 208109, New Haven, CT 06520-8109, USA

F. Hervé
Departamento de Geología, Universidad de Chile,
Plaza Ercilla 803, Casilla 13518 Correo 21, Santiago, Chile

Keywords Southern Chilean Andes · Liquiñe-Ofqui Fault Zone · Fission track thermochronology · Arc magmatism · Denudation

Introduction

The Southern Chilean Andes are a segment of the orogen at the western margin of South America that is affected by the subduction of a spreading oceanic ridge (Fig. 1). At the active margin, the present-day intersection of the Chile rise between the Nazca and the Antarctic plates and the Peru–Chile trench defines the Chile triple junction (CTJ), situated currently at ~46°30′S. Plate tectonic reconstructions for the east Pacific Ocean floor indicate that convergence along the South American margin has retained an E to NE direction during most of the Cenozoic (Cande and Leslie 1986; Pardo-Casas and Molnar 1987; Somoza 1998). Subduction of the Chile Rise beneath the southernmost tip of the South American plate began between ~14 Myr and 10 Myr ago (Cande and Leslie 1986). The similar orientations of the ridge and the Peru–Chile trench resulted in the CTJ migrating ca. 700 km northwards to its present-day position.

As an apparent effect of the oblique ridge subduction, different structural domains along the Andean orogen characterise differences in the geodynamic situation north and south of the CTJ (Dewey and Lamb 1992; Diriason et al. 1998; Lavenu and Cembrano 1999; Thomson et al. 2001). North of the triple junction, the most prominent structure in the overriding plate is the Liquiñe-Ofqui fault zone (LOFZ), which stretches along the Main Range more than 950 km from Golfo de Penas to about 39°S (Hervé 1976, 1979; Cembrano et al. 1996, 2000, 2002).

The activity of the LOFZ has been interpreted as right-lateral strike-slip partition of strain in the thermally weakened lithosphere of the arc region driven by northward-oblique subduction (Hervé 1976; Beck et al. 1993, 2000; Rojas et al. 1994; Cembrano et al. 1996, 2000, 2002). Other authors invoke an effect of indention

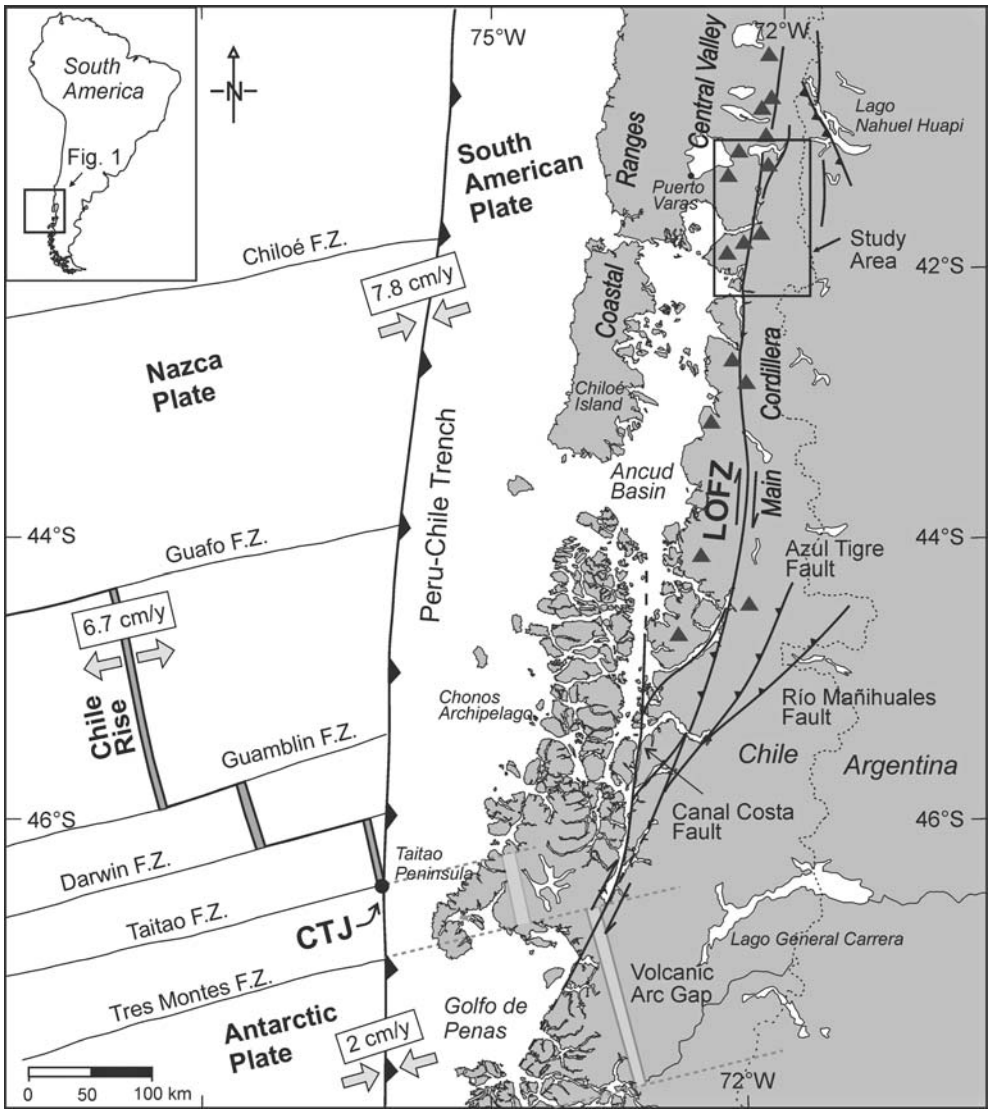

Fig. 1 Plate tectonic setting of the southern Chilean Andes and location of the study area. *CTJ*: Chile Triple Junction. LOFZ: Liquiñe-Ofqui fault zone. *Solid triangles* represent the location of active volcanoes. *Arrows* represent directions of diverging and converging plate boundaries (after Thomson et al. 2001)

of the Chile ridge into the South American margin in the past 14 Myr (Forsythe and Nelson 1985; Forsythe et al. 1986; Murdie et al. 1993; Nelson et al. 1994). In their model, the subduction of the active ridge caused an outboard sliver in the forearc, the so-called Chiloé block, to become detached from the continental margin along the right-lateral LOFZ. Geodynamic and palaeomagnetic studies suggest that the displacement of this block is buttressed to the north of ~40°S, where subduction beneath the Central Andes is flat and the South American margin is more concave towards the ENE (Beck et al. 1993, 2000; Lavenu and Cembrano 1999; Vietor and Echtler 2005). Total amounts of displacements along the LOFZ remain largely unknown owing mostly to the lack of easily identifiable offset geological markers, the lack of detailed geological maps and the relatively monotonous distribution of the main geologic units outcropping along its traces.

Structural mapping, microfabric analyses, Ar-Ar geochronology, and more recently, fission track (FT) thermochronology along the Patagonian Andes between ~42° and 47°S provide evidence for right-lateral transpression along the LOFZ in the late Cenozoic (Cembrano et al. 2000, 2002; Thomson et al. 2001; Thomson 2002).

The long-lived activity of the LOFZ is closely related with the episodic evolution of the magmatic arc of the southern Andes, represented by the North Patagonian Batholith (NPB, Hervé 1984; Munizaga et al. 1988; Pankhurst et al. 1992, 1999). Information on the age and distribution of plutons of the NPB in the Chiloé and Los Lagos regions of Chile is available through mapping campaigns and geochronology performed by the Universidad de Chile (Munizaga et al. 1988; Carrasco 1995), and more recently Sernageomin (Sernageomin-BRGM 1995; Duhart et al. 2000). Apart from isolated Al-in-hornblende geobarometry reports (Hervé et al. 1996; Seifert et al. 2003), few details are known about the post-emplacement cooling and exhumation histories of the plutons building the NPB. The subject of this paper is to report 107 new fission-track (FT) ages from the Main Range of the Southern Andes between ~41°S and

42°15′S, revealing the different emplacement and cooling histories of the plutons building the NPB in the region. Their denudation in relation to the late Cenozoic activity of the LOFZ is also explored.

Geological framework

The southern Chilean Andes can be divided into three main morphologic units (from west to east, Figs. 1, 2):

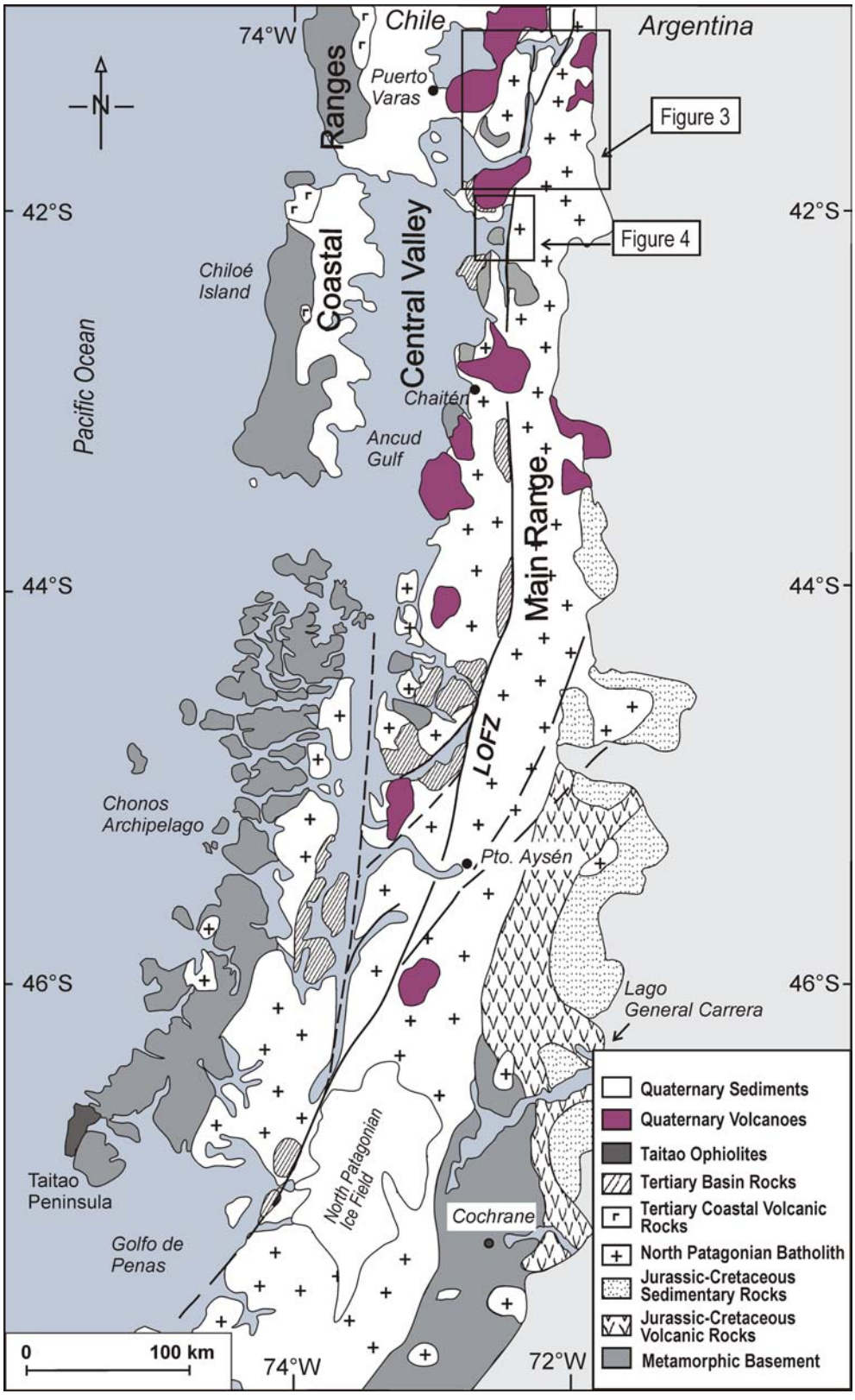

Fig. 2 Simplified geological map of the southern Chilean Andes between 41°S and 48°S after Sernageomin (1980) and Hervé et al. (2000)

the Coastal Ranges, the Central Valley (or Ancud Basin south of 41°S), and the Main Range. The regional geology is dominated by calk-alkaline plutonic rocks of the Meso-Cenozoic Patagonian Batholith (Fig. 2), which extends as a continuous belt along the Main Range between latitudes 40°S and 53°S. The segment of the batholith north of ~47°S, the so-called North Patagonian Batholith (NPB), intruded a late Palaeozoic to early Mesozoic metamorphic accretionary wedge complex at the eastern margin of the Coastal Ranges (Hervé et al. 1999, 2000; Hervé and Fanning 2001; Martin et al. 1999; Duhart et al. 2000), Jurassic silicic volcanic rocks of the Ibañez Formation towards the eastern flank of the Main Range (Pankhurst et al. 1998, 1999), and the overlying early Cretaceous shallow marine volcano-sedimentary rocks of the Aysén basin (De la Cruz et al. 1996; Suarez and De la Cruz 2000). The NPB has been shown to display an episodic magmatic history with predominantly late Jurassic to mid Cretaceous ages at its western and eastern margins and early Miocene to Pliocene ages in the centre (Hervé 1984; Munizaga et al. 1988; Pankhurst et al. 1992, 1999). The discrete episodes of magmatism appear to correspond with increased rates of plate convergence and decreasing angles of obliquity with respect to the Peru–Chile trench (Pankhurst et al. 1999). A pause in plutonism during early Tertiary times coincides with a phase of regional extension, volcanism, and sedimentation along the Coastal Ranges and the Central Valley between 36°S and ~43°S (Muñoz et al. 2000). Enclosed by the main strands of the LOFZ, several marine volcano-sedimentary basins sit unconformably on eroded parts of the NPB and are locally intruded by younger late Miocene plutons (e.g. Ayacara Formation, Rojas et al. 1994; Traiguén Formation, Hervé et al. 1995). These are interpreted as pull-apart basins formed at dextral-releasing offsets of the LOFZ. The Late Miocene plutons, sporadically exposed near the traces of the LOFZ, have been described as syntectonic (Hervé et al. 1993; Pankhurst et al. 1992, 1999). Along the LOFZ, centimetre- to meter-thick mylonitic bands are found within the plutonic rocks. According to Ar-Ar dating by Cembrano et al. (2000, 2002), many of these mylonites were formed in late Miocene to Pliocene times. Starting from Pliocene times, and during most of the Quaternary, expansive glaciation has affected much of the Patagonian Andes (Mercer and Sutter 1982; Rabassa and Clapperton 1990; Singer et al. 2004). Glaciation extended to the Pacific coast until ~20,000 years ago and eastwards into the extra-Andean Patagonia where well-developed moraine systems persist (Heusser 1990; Lliboutry 1999). Because of the limited access to the outcrops in the study region, sampling for FT analysis was carried out in two specific areas of the Main Range; additionally, these areas show differences in the age distribution and deformation conditions of plutons exposed along the fault zone. The thermochronologic results are consequently analysed and discussed separately for each area in the following sections.

The North Patagonian Batholith in the Reloncaví area

The distribution of Miocene and Cretaceous plutons of the NPB in the Reloncaví area is shown in more detail together with a compilation of available geochronologic and geobarometric data in Fig. 3. The ages of the plutons are, in most cases, constrained by K-Ar and Ar-Ar dates (Munizaga et al. 1988; Carrasco 1995; Sernageomin-BRGM 1995), which depending on the level of emplacement do not necessarily correspond to the intrusion ages (Faure 1986). Two N-NNE diverging fault segments of the LOFZ appear to juxtapose Miocene and Cretaceous plutons with sharp contacts along the Reloncaví Estuary and the southern branch of the Todos Los Santos Lake. The main strand trends approximately N–S and follows the regional orientation of the fault zone. The second is oblique to the main segment and of limited extent, suggesting an origin as a large-scale dextral Riedel shear (Tchalenko 1970). Assuming that the Cretaceous plutons across the fault zone were emplaced simultaneously and originally formed a coherent intrusive complex, a dextral displacement of ~30 km is inferred from the relative position of Miocene and Cretaceous plutons along the Reloncaví Estuary, comparable to the size of pull-apart basins south of the study area (Fig. 2). Al-in hornblende geobarometry indicates crystallisation depths of between ~8 km and ~14 km, with deeper levels of emplacement for the plutons located west of the LOFZ (Seifert et al. 2003). Along the traces of the LOFZ, the plutonic rocks are generally unfoliated and at best weakly deformed (Adriasola 2003). To the west of the LOFZ, contact metamorphic associations of andalusite, K-feldspar, and sillimanite have been reported within gneisses of the metamorphic basement (Thiele et al. 1986; Parada et al. 1987). This assemblage is indicative of low-pressure conditions (< 0.3 GPa, Holdaway 1971; Spear and Cheney 1989), suggesting a shallow level of emplacement for the intruding Miocene plutons in these sectors.

The North Patagonian Batholith in the Hornopirén area

A geologic map of the Hornopirén area is shown in Fig. 4, including available geochronologic and geobarometric data from the region. A small plutonic complex of late Miocene to Pliocene age is emplaced into Cretaceous parts of the NPB, pelitic schists of the metamorphic basement, and dacitic tuffs of the Tertiary Ayacara Formation (Hervé et al. 1979; Pankhurst et al. 1992; Rojas et al. 1994). Plutonic rocks with different conditions of deformation are exposed along the LOFZ (Cembrano et al. 1996, 2000; Adriasola 2003). Tonalites of Miocene age outcropping along the eastern border of the LOFZ between Río Mariquita and Pichanco display zones with a pronounced fault-related foliation overprinting an earlier magmatic foliation. The tectonic foliation is roughly oriented in NNW direction and in

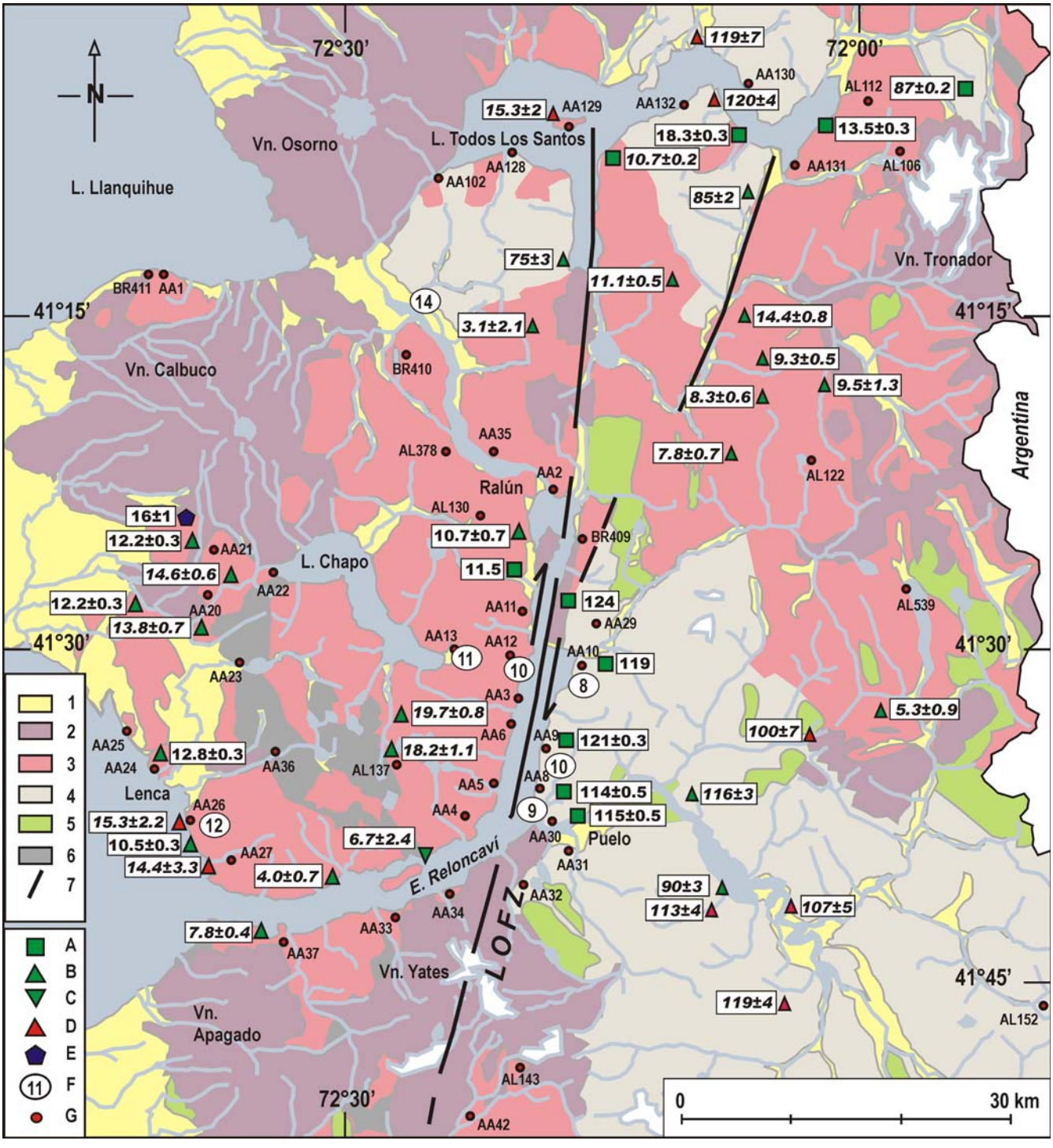

Fig. 3 Geology of the Reloncaví area (after Duhart et al. 2000): *1* Quaternary sediments. *2* Quaternary volcanic deposits. *3* Miocene plutonic rocks. *4* Cretaceous plutonic rocks. *5* Jurassic-Cretaceous volcano-sedimentary rocks. *6* Metamorphic basement rocks. *7* Liquiñe-Ofqui fault zone. Compiled isotopic ages (Ma) after Carrasco (1995), Munizaga et al. (1988), and Sernageomin-BRGM (1995). *A* Ar-Ar biotite. *B* K-Ar biotite. *C* K-Ar whole rock. *D* K-Ar hornblende. *E* Rb-Sr whole rock. *F* Al-in-Hornblende crystallisation depth (km). *G* Samples for FT dating (with sample number). Abbreviations in map: *Vn* Volcán, *E* Estero, *L* Lago

general dips steeply to the E. The continuation of this structural imprint to the north was observed beyond the outcrops of the plutons, affecting metamorphic and pyroclastic rocks near Río Negro, and to the south near Pichanco. The microstructures and mineral assemblages of the foliated tonalites show ductile fabrics formed at greenschist facies conditions (Cembrano et al. 2000; Adriasola 2003). A sample of a dark-coloured shear zone near Río Mariquita revealed S-C fabrics (Lister and Snoke 1984; Dell'Angelo and Tullis 1989), indicat-

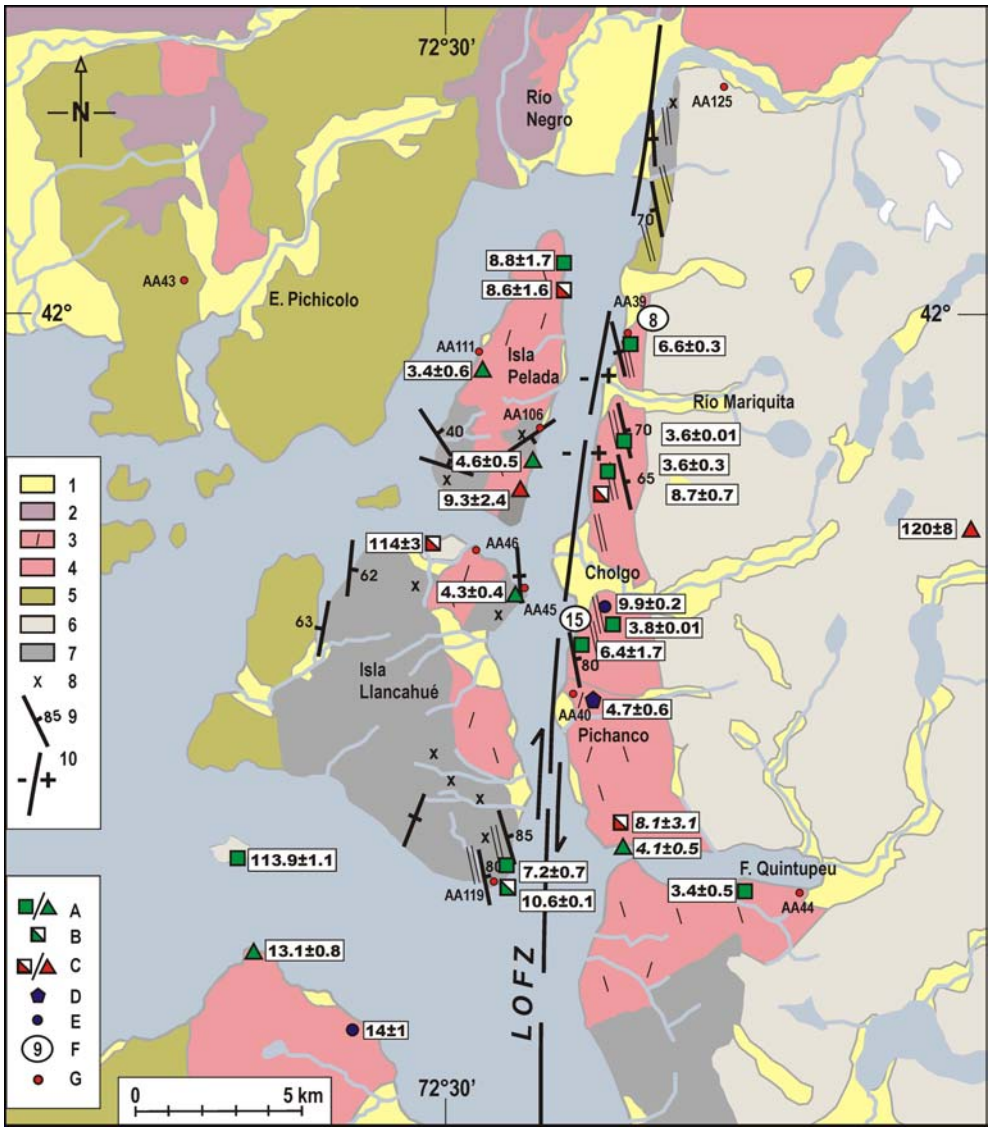

Fig. 4 Geology of the Hornopirén area (modified after Cembrano et al. 1996). *1* Quaternary sediments. *2* Quaternary volcanic deposits. *3* Unfoliated Late Miocene and Pliocene plutonic rocks. *4* Miocene plutonic rocks. *5* Mid-Tertiary volcanic rocks. *6* Cretaceous plutonic rocks. *7* Metamorphic basement rocks. *8* Areas with contact metamorphism. *9* Strike/dip of foliation. *10* Areas of relative block uplift. Compiled isotopic ages (Ma) after Cembrano et al. (2000), Pankhurst et al. (1992) and Sernageomin-BRGM (1995). *A* Ar-Ar/K-Ar biotite. *B* Ar-Ar muscovite. *C* Ar-Ar/K-Ar hornblende. *D* Rb-Sr whole rock. *E* U-Pb zircon. *F* Al-in-Hornblende crystallisation depths (km) after Seifert et al. (2003) and Hervé et al. (1996). *G* Samples for FT dating (with sample number)

ing a dip-slip displacement with the relative upward displacement of the eastern block (Adriasola 2003). For the uplifted tonalite unit, Al-in-hornblende geobarometry data indicate maximum crystallisation depths of ~8 km and ~15 km (Hervé et al. 1996; Seifert et al. 2003). At Cholgo, one U-Pb intrusion age of 10 Ma (Cembrano et al. 2000) constrains the time of emplacement for the deformed tonalites. Further south, near Pichanco, an Rb-Sr isochron of 5 Ma has been reported by Pankhurst et al. (1992) for undeformed coarse-grained tonalites and associated granodiorites, suggesting different magmatic events to have occurred along the eastern side of the fault zone (Cembrano et al. 2000). Plutons located at the western side of the LOFZ are predominantly dioritic to tonalitic in composition. These are generally unfoliated and at best weakly deformed (Adriasola 2003). Outcrops of quartz-mica schists at the southeastern shore of Llancahué Island display a very regular NNW-trending and steeply dipping foliation, following the general tectonic grain. The metamorphic basement rocks on other parts of the island display a more irregular foliation, locally disrupted by contact aureoles. Contact metamorphic assemblages with andalusite, cordierite, and sillimanite have been reported within aureoles of the basement rocks on Llancahué Island (Pankhurst et al. 1992). These phase assemblages are indicative of low-pressure conditions (<0.3 GPa; Holdaway 1971; Spear and Cheney 1989) and shallow level of emplacement for the plutons west of the LOFZ.

Fission-track thermochronology

Sampling procedure and methods

Sampling for FT thermochronology was organised to be as widespread as possible in order to observe variations of the cooling histories of the plutonic units of the NPB

Table 1 Fission Track results from the Main Andean Range of Chile between 41°S and 42°15′S[a]

Sample number	Location latitude; longitude[b]	Elevation (m)	Rock type	Mineral	Number of crystals	Track density ($\times 10^6$ tr·cm^2)			Age dispersion ($P(\chi^2)$)	Central age (Ma) ($\pm 1\sigma$)	Apatite length (μm $\pm$ 1σ)	Number of tracks	Standard deviation (μm)
						ρ_s (N_S)	ρ_i (N_i)	ρ_d (N_d)					
AA1*	Lago Llanquihue 41°12′58″S; 72°40′13″W	80 m	Granodiorite	Apatite	20	0.074 (32)	0.762 (328)	1.508 (10,415)	< 1% (98%)	24.9 ± 4.7	–	–	–
				Zircon	20	2.295 (970)	2.754 (1,164)	0.391 (5,395)	< 1% (83%)	21.2 ± 1.0			
AA2*	Ralún 41°22′55″S; 72°18′11″W	30 m	Tonalite	Apatite	20	0.167 (69)	9.853 (4,082)	1.516 (10,467)	< 1% (99%)	4.4 ± 0.5	13.71 ± 0.21	76	1.79
				Zircon	20	1.412 (1026)	2.949 (2,142)	0.390 (5,386)	< 1% (65%)	12.2 ± 0.5			
AA3*	E. Reloncaví 41°32′10″S; 72°20′06″W	60 m	Tonalite	Apatite	20	0.029 (8)	1.342 (367)	1.523 (10,519)	< 1% (100%)	5.6 ± 2.0	14.81 ± 0.22	26	1.08
				Zircon	20	2.958 (3,117)	5.233 (5,514)	0.390 (5,390)	12% (< 1%)	14.1 ± 0.6			
AA4*	E. Reloncaví 41°36′24″S; 72°23′08″W	20 m	Tonalite	Apatite	18	0.116 (20)	8.094 (1,386)	1.531 (10,572)	< 1% (97%)	3.8 ± 0.9	–	–	–
				Zircon	20	0.767 (522)	2.402 (1,642)	0.392 (5,408)	19% (6%)	8.0 ± 0.6			
AA6*	E. Reloncaví 41°34′14″S; 72°20′45″W	20 m	Tonalite	Apatite	20	0.054 (18)	3.513 (1,247)	1.546 (10,677)	14% (53%)	3.8 ± 0.9	14.10 ± 0.29	15	1.08
				Zircon	20	0.719 (1,267)	1.733 (3,054)	0.389 (5,678)	22% (< 1%)	10.5 ± 0.7			
AA8*	E. Reloncaví 41°36′59″S; 72°18′40″W	80 m	Granodiorite	Apatite	20	0.052 (33)	4.149 (2,636)	1.554 (10,729)	1% (77%)	3.3 ± 0.6	14.45 ± 0.29	24	1.39
AA9*	E. Reloncaví 41°34′22″S; 72°18′32″W	110 m	Granite	Apatite	20	0.054 (21)	4.162 (1,592)	1.561 (10,781)	< 1% (98%)	3.5 ± 0.8	14.76 ± 0.50	12	1.65
				Zircon	20	2.238 (5,399)	0.615 (1,418)	0.388 (5,361)	1% (60%)	91.6 ± 3.3			
AA10*	Cochamo 41°30′33″S; 72°16′35″W	100 m	Granite	Zircon	20	3.973 (5,701)	1.329 (1,907)	0.383 (5,290)	4% (22%)	74.2 ± 2.6			
AA11*	E. Reloncaví 41°26′55″S; 72°19′57″W	150 m	Granodiorite	Apatite	20	0.013 (8)	1.052 (655)	1.569 (10,834)	< 1% (94%)	3.3 ± 1.2	14.18 ± 0.35	21	1.56
				Zircon	20	0.665 (1,016)	2.101 (3,209)	0.388 (5,352)	17% (< 1%)	8.0 ± 0.5			
AA12*	Canutillar 41°30′15″S; 72°20′35″W	180 m	Tonalite	Apatite	14	0.066 (10)	4.391 (667)	1.576 (10,886)	< 1% (90%)	4.0 ± 1.3	14.77 ± 0.64	6	1.43
				Zircon	20	0.808 (849)	2.045 (1,971)	0.387 (5,344)	4% (48%)	10.9 ± 0.5			
AA13*	L. Chapo 41°30′00″S;72°22′39″W	300 m	Tonalite	Apatite	16	0.218 (34)	12.16 (1,897)	1.584 (10,938)	< 1% (99%)	4.8 ± 0.8	–	–	–
				Zircon	7	2.359 (303)	0.507 (651)	0.386 (5,355)	5% (35%)	11.7 ± 0.9			
AA20*	Correntoso 41°27′42″S; 72°37′40″W	200 m	Granodiorite	Apatite	16	0.065 (42)	1.604 (1,037)	1.614 (11,148)	1% (71%)	11.1 ± 1.8	–	–	–
				Zircon	20	2.824 (2,211)	4.698 (3,679)	0.384 (5,299)	2% (50%)	15.1 ± 0.5			
AA21*	L. Chapo 41°25′41″S; 72°37′20″W	250 m	Granodiorite	Apatite	20	0.095 (62)	2.283 (1,491)	1.621 (11,200)	1% (60%)	11.4 ± 1.5	13.14 ± 0.85	7	2.08
				Zircon	20	2.236 (2,436)	4.527 (4,933)	0.386 (5,326)	14% (< 1%)	12.4 ± 0.6			

Table 1 (Contd.)

Sample number	Location latitude; longitude[b]	Elevation (m)	Rock type	Mineral	Number of crystals	Track density ($\times 10^6$ tr·cm^2)			Age dispersion (P(χ^2))	Central age (Ma) ($\pm 1\sigma$)	Apatite length (μm $\pm$ 1σ)	Number of tracks	Standard deviation (μm)
						ρ_s (N_S)	ρ_i (N_i)	ρ_d (N_d)					
AA22*	L. Chapo 41°26′41″S; 72°33′49″W	300 m	Granodiorite	Apatite	20	0.154 (105)	3.887 (2,657)	1.629 (11,252)	6% (57%)	10.9 ± 1.1	–	–	–
				Zircon	20	2.612 (2,211)	5.026 (4,255)	0.386 (5,327)	10% (2%)	12.9 ± 0.5			
AA23*	L. Chaiquenes 41°30′38″S; 72°35′44″W	450 m	Gneiss	Apatite	20	0.143 (72)	4.947 (2,487)	1.637 (11,305)	9% (90%)	8.0 ± 1.0	14.29 ± 0.13	100	1.32
				Zircon	20	1.267 (560)	3.799 (1,679)	0.385 (5,318)	13% (14%)	8.3 ± 0.5			
AA24*	Punta Metri 41°35′20″S; 72°40′32″W	10 m	Granodiorite	Apatite	20	0.024 (24)	2.754 (715)	1.644 (11,357)	< 1% (99%)	9.4 ± 2.0	14.54 ± 0.20	85	1.79
				Zircon	20	0.839 (2,717)	1.494 (3,590)	0.376 (5,190)	11% (1%)	13.7 ± 0.6			
AA25*	Punta Metri 41°33′33″S; 72°42′27″W	20 m	Tonalite	Apatite	20	0.096 (65)	2.155 (1,458)	1.652 (11,410)	< 1% (92%)	12.5 ± 1.6	14.72 ± 0.14	77	1.26
				Zircon	20	0.829 (913)	1.883 (2,072)	0.387 (5,345)	3% (32%)	11.1 ± 0.5			
AA26*	Caleta Larenas 41°37′38″S; 72°38′38″W	10 m	Tonalite	Apatite	20	0.225 (76)	8.134 (2,752)	1.66 (11,462)	< 1% (77%)	7.8 ± 0.9	13.63 ± 0.19	80	1.65
				Zircon	19	1.232 (854)	2.992 (2,074)	0.385 (5,317)	9% (22%)	9.3 ± 0.4			
AA27*	Caleta Larenas 42°39′24″S; 72°36′23″W	200 m	Tonalite	Apatite	20	0.268 (140)	8.118 (4,238)	1.667 (11,514)	< 1% (95%)	9.3 ± 0.8	13.77 ± 0.21	100	2.05
				Zircon	19	0.688 (978)	1.584 (2,251)	0.383 (5,284)	8% (25%)	10.8 ± 0.5			
AA29*	Rio Cochamo 41°28′44″S; 72°15′38″W	150 m	Granite	Apatite	20	0.094 (43)	4.849 (2,230)	1.675 (11,567)	1% (73%)	5.5 ± 0.9	15.03 ± 0.28	15	1.16
				Zircon	20	4.924 (6,297)	1.848 (2,363)	0.381 (5,263)	6% (10%)	65.9 ± 2.3			
AA30*	Balseo 41°37′38″S; 72°18′11″W	100 m	Tonalite	Apatite	20	0.027 (19)	1.963 (1,361)	1.682 (11,619)	2% (52%)	4.0 ± 0.9	14.38 ± 0.28	30	1.49
				Zircon	20	5.427 (5,614)	1.543 (1,596)	0.384 (5,301)	31% (< 1%)	85.9 ± 6.8			
AA31*	Puelo Chico 41°39′02″S; 72°17′14″W	250 m	Granite	Apatite	20	0.031 (19)	2.233 (1,360)	1.690 (11,671)	1% (86%)	4.0 ± 0.9	–	–	–
				Zircon	20	5.311 (4,973)	1.793 (1,679)	0.391 (5,399)	20% (< 1%)	73.0 ± 4.2			
AA32*	Puelo 41°40′23″S; 72°19′47″W	300 m	Granite	Apatite	20	0.025 (9)	2.093 (766)	1.697 (11,724)	1% (97%)	3.4 ± 1.4	–	–	–
				Zircon	20	7.377 (4,592)	2.961 (1,123)	0.378 (5,217)	17% (< 1%)	62.0 ± 3.0			
AA33*	Volcán Yates 41°41′57″S; 72°27′08″W	20 m	Granodiorite	Apatite	30	0.150 (125)	7.022 (5,857)	1.552 (11,004)	< 1% (80%)	5.5 ± 0.5	15.03 ± 0.19	40	1.21
				Zircon	20	0.469 (600)	2.368 (2,857)	0.388 (5,308)	2% (44%)	5.3 ± 0.3			
AA34*	Volcán Yates 41°40′41″S; 72°23′56″W	30 m	Tonalite	Apatite	20	0.123 (72)	7.647 (4,488)	1.559 (11,196)	< 1% (97%)	4.2 ± 0.5	14.11 ± 0.14	52	1.03
				Zircon	20	0.431 (1,040)	1.642 (3,963)	0.383 (5,293)	9% (12%)	6.6 ± 0.3			

Table 1 (Contd.)

Sample number	Location latitude; longitude[b]	Elevation (m)	Rock type	Mineral	Number of crystals	Track density ($\times 10^6$ tr·cm^2) ρ_s (N_S)	ρ_i (N_i)	ρ_d (N_d)	Age dispersion ($P(\chi^2)$)	Central age (Ma) ($\pm 1\sigma$)	Apatite length (μm $\pm$ 1σ)	Number of tracks	Standard deviation (μm)
AA35*	Termas de Ralún 41°21′06″S; 72°21′32″W	150 m	Tonalite	Apatite	20	0.186 (58)	8.017 (2,502)	1.566 (11,387)	2% (64%)	6.2 ± 0.8	14.84 ± 0.30	16	1.17
				Zircon	20	0.606 (541)	1.268 (1,133)	0.380 (5,254)	< 1% (73%)	11.9 ± 0.7			
AA36*	Parque Alerce Andino 41°34′34″S; 72°33′08″W	200 m	Gneiss	Apatite	20	0.211 (40)	6.866 (1,299)	1.573 (11,579)	< 1% (96%)	8.2 ± 1.3	13.85 ± 0.45	17	1.79
				Zircon	20	1.518 (870)	4.821 (2,763)	0.390 (5,381)	11% (10%)	8.0 ± 0.4			
AA37*	Chaparrano 41°43′43″S; 72°33′21″W	30 m	Tonalite	Apatite	20	0.0590 (53)	2.315 (2,081)	1.580 (11,771)	5% (62%)	6.8 ± 1.0	13.77 ± 0.16	88	1.48
				Zircon	20	0.623 (1,017)	1.928 (3,150)	0.388 (5,354)	18% (1%)	8.2 ± 0.5			
AA39*	Rio Mariquita 42°01′20″S; 72°26′47″W	150 m	Tonalite, foliated	Apatite	20	0.034 (9)	1.582 (426)	1.587 (11,963)	< 1% (97%)	5.7 ± 1.9	–	–	–
				Zircon	20	0.176 (319)	0.732 (1,326)	0.377 (5,199)	16% (17%)	6.1 ± 0.5			
AA40*	Pichanco 42°06′46″S; 72°27′37″W	40 m	Granodiorite	Apatite	20	0.098 (33)	6.106 (2,066)	1.594 (12,155)	< 1% (98%)	4.3 ± 0.7	14.87 ± 0.20	49	1.37
				Zircon	20	0.341 (632)	2.103 (3,895)	0.382 (5,276)	19% (2%)	3.8 ± 0.3			
AA42*	Rio Negro 41°50′51″S; 72°22′39″W	200 m	Tonalite	Apatite	18	0.044 (13)	1.254 (369)	1.601 (12,347)	> 99% (78%)	4.2 ± 2.7	13.4 ± 0.46	9	1.30
				Zircon	20	0.861 (776)	4.236 (3,820)	0.381 (5,267)	33% (< 1%)	4.8 ± 0.4			
AA43*	Pichicolo 41°59′36″S; 72°36′20″W	100 m	Dacite	Apatite	20	0.0418 (37)	0.723 (640)	1.607 (12,539)	< 1% (97%)	15.5 ± 2.7	14.71 ± 0.22	35	1.30
				Zircon	20	0.420 (1,049)	1.874 (1,795)	0.382 (5,272)	< 1% (89%)	14.6 ± 0.6			
AA44*	F. Quintupeu 42°10′15″S; 72°27′30″W	10 m	Tonalite	Apatite	20	0.070 (62)	5.851 (5,220)	1.614 (12,730)	31% (15%)	3.3 ± 0.5	13.67 ± 0.20	52	1.40
				Zircon	20	0.742 (1,049)	4.174 (5,903)	0.378 (5,208)	12% (2%)	4.4 ± 0.2			
AA45*	I.Llancahué 42°04′17″S; 72°28′40″W	5 m	Mica-schist	Apatite	18	0.069 (14)	4.369 (887)	1.621 (12,922)	< 1% (82%)	4.3 ± 1.2	14.11 ± 0.44	8	1.17
				Zircon	20	0.253 (659)	1.943 (5,076)	0.382 (5,281)	27% (< 1%)	3.2 ± 0.5			
AA46*	I.Llancahué 42°03′53″S; 72°29′50″W	5 m	Tonalite	Zircon	20	0.393 (656)	2.129 (3,555)	0.380 (5,250)	20% (< 1%)	4.5 ± 0.3			
AA102**	Petrohué 41°08′38″S; 72°24′44″W	50 m	Tonalite	Apatite	20	0.026 (9)	1.015 (356)	1.504 (10,380)	< 1% (97%)	6.3 ± 2.2	–	–	–
				Zircon	20	0.674 (393)	3.863 (2,251)	0.399 (5,510)	< 1% (94%)	4.5 ± 0.3			
AA106**	Isla Pelada 42°01′50″S; 72°29′43″W	5 m	Tonalite	Apatite	12	0.063 (10)	3.709 (589)	1.496 (10,330)	39% (34%)	4.3 ± 1.5	–	–	–
				Zircon	20	0.427 (385)	3.034 (2,736)	0.402 (5,550)	28% (< 1%)	3.4 ± 0.3			

Table 1 (Contd.)

Sample number	Location atitude; longitude[b]	Elevation (m)	Rock type	Mineral	Number of crystals	Track density ($\times 10^6$ tr·cm^2)			Age dispersion (P(χ^2))	Central age (Ma) ($\pm 1\sigma$)	Apatite mean track length (μm $\pm$ 1σ)	Number of tracks	Standard deviation (μm)
						ρ_s (N_S)	ρ_i (N_i)	ρ_d (N_d)					
AA111**	Isla Pelada 42°00′59″S; 72°27′43″W	5 m	Aplite	Apatite	15	0.084 (14)	4.734 (791)	1.489 (10,280)	< 1% (70%)	4.4 ± 1.2	–	–	–
				Zircon	20	0.509 (456)	3.534 (3,167)	0.416 (5,747)	21% (1%)	3.9 ± 0.3			
AA119**	Isla Llancahué 42°09′40″S; 72°29′16″W	5 m	Mica-schist	Apatite	16	0.012 (8)	0.598 (404)	1.474 (10,179)	1% (64%)	4.9 ± 1.7	–	–	–
AA125**	Rio Blanco 41°56′55″S; 72°23′05″W	100 m	Granite	Apatite	20	0.125 (32)	4.814 (1,230)	1.460 (10,078)	16% (7%)	6.5 ± 1.2	14.83 ± 0.15	100	1.53
AA128**	Lago Todos Los Santos 41°07′44″S; 72°20′25″W	5 m	Granite	Zircon	10	5.538 (2,394)	2.133 (922)	0.400 (5,530)	11% (3%)	67.0 ± 3.8			
AA129**	Lago Todos Los Santos 41°06′44″S; 72°17′14″W	5 m	Granite	Apatite	20	0.069 (56)	3.883 (3,142)	1.445 (9,978)	19% (57%)	4.4 ± 0.6	14.38 ± 0.21	39	1.28
				Zircon	20	0.488 (412)	3.417 (2,883)	0.413 (5,707)	7% (23%)	3.8 ± 0.2			
AA130**	Lago Todos Los Santos 41°04′34″S; 72°07′10″W	5 m	Granite	Apatite	20	1.324 (68)	5.217 (2,680)	1.438 (9,928)	< 1% (96%)	6.1 ± 0.8	14.56 ± 0.13	99	1.29
				Zircon	20	1.591 (1,433)	2.357 (2,122)	0.418 (5,767)	23% (< 1%)	17.7 ± 1.1			
AA131**	Lago Todos Los Santos 41°08′16″S; 72°04′18″W	20 m	Tonalite	Apatite	20	0.053 (31)	2.726 (2,033)	0.409 (5,648)	< 1% (85%)	6.9 ± 1.3	14.41 ± 0.28	36	1.63
				Zircon	20	1.395 (1,040)	1.849 (1,080)	1.431 (9,877)	16% (1%)	13.8 ± 0.8			
AA132**	Lago Todos Los Santos 41°05′30″S; 72°10′51″W	10 m	Tonalite	Apatite	20	0.046 (19)	1.650 (688)	0.419 (5,786)	38% (12%)	7.2 ± 1.8	14.88 ± 0.39	12	1.29
				Zircon	10	6.411 (3,152)	1.886 (927)	1.511 (10,430)	19% (2%)	93.3 ± 6.9			
AL106**	Monte Tronador 41°09′48″S; 71°58′12″W	750 m	Granite	Zircon	4	0.997 (73)	3.019 (221)	0.406 (18)	1% (24%)	8.7 ± 1.2			
AL112**	Volcan Casablanca 41°05′20″S; 71°59′32″W	850 m	Tonalite	Apatite	21	0.023 (77)	5.330 (1,796)	0.408 (5,628)	< 1% (53%)	10.6 ± 1.3	14.40 ± 0.16	100	1.54
				Zircon	20	0.536 (362)	1.459 (985)	1.482 (10,229)	8% (34%)	9.8 ± 0.7			
AL122**	Rio Cochamo 41°21′21″S; 72°03′30″W	1,600 m	Tonalite	Apatite	20	0.044 (19)	1.630 (698)	1.467 (10,129)	4% (44%)	6.7 ± 1.6	14.32 ± 0.28	26	1.42
AL130**	Cochamo 41°23′54″S; 72°22′20″W	1,400 m	Granite	Zircon	20	0.413 (354)	0.807 (692)	0.403 (5,569)	< 1% (90%)	13.4 ± 0.9			
AL137**	Puelo 41°34′18″S; 72°25′12″W	1,200 m	Granodiorite	Apatite	20	0.149 (31)	1.448 (878)	1.658 (11,445)	18% (64%)	9.8 ± 1.9	14.44 ± 0.18	76	1.57
				Zircon	20	0.737 (553)	1.168 (876)	0.412 (5,688)	10% (63%)	16.8 ± 1.1			
AL143**	Rio Traidor 41°48′48″S; 72°20′06″W	1,000 m	Tonalite	Zircon	20	7.028 (2,174)	2.189 (677)	0.420 (5,806)	< 1% (99%)	87.6 ± 4.2			
AL152**	Llanada Grande 41°50′06″S; 71°50′26″W	1,550 m	Tonalite	Apatite	20	0.040 (17)	1.600 (685)	0.423 (5,865)	4% (44%)	6.7 ± 1.7	13.75 ± 0.60	6	1.60

Table 1 (Contd.)

Sample number	Location latitude; longitude[b]	Elevation (m)	Rock type	Mineral	Number of crystals	Track density ($\times 10^6$ tr·cm^2)			Age dispersion (P(χ^2))	Central age (Ma) ($\pm 1\sigma$)	Apatite length (μm $\pm$ 1σ)	Number of tracks	Standard deviation (μm)
						ρ_s (N_S)	ρ_i (N_i)	ρ_d (N_d)					
				Zircon	20	6.046 (3,181)	1.492 (785)	1.624 (10,280)	18% (<1%)	110.6 ± 8.1			
AL169**	Arroyo Ventisquero 41°46′02″S; 72°05′6″W	1,800 m	Granite	Apatite	20	0.078 (43)	1.793 (988)	0.405 (5,589)	<1% (70%)	11.7 ± 1.9	14.58 ± 0.22	33	1.27
				Zircon	20	6.446 (4,184)	2.126 (1,380)	1.613 (11,136)	<1% (90%)	79.3 ± 2.9			
AL181**	Cholgo 42°12′06″S; 72°16′12″W	1,200 m	Tonalite	Apatite	20	0.189 (34)	9.690 (2,770)	1.602 (11,059)	0% (90%)	3.3 ± 0.6	14.46 ± 0.29	37	1.73
				Zircon	20	0.356 (464)	1.297 (1,693)	0.398 (5,490)	15% (9%)	7.1 ± 0.5			
AL378**	Cochamó 41°20′48″S; 72°23′30″W	100 m	Granite	Apatite	20	0.209 (76)	8.615 (3,129)	1.591 (10,904)	8% (50%)	6.4 ± 0.8	13.87 ± 0.83	6	1.85
				Zircon	20	1.372 (1,652)	2.662 (3,206)	0.410 (5,668)	10% (7%)	13.5 ± 0.6			
AL539**	Lago Vidal Gormaz 41°27′12″S; 71°58′05″W	600 m	Ganodiorite	Apatite	12	0.0637 (12)	3.040 (382)	1.579 (10,904)	<1%(88.5%)	5.5 ± 2.0	–	–	–
				Zircon	20	0.6319 (233)	4.488 (1,255)	0.415 (5,767)	12% (55%)	3.8 ± 0.3			
BR409***	Pte. Las Trancas, Ralún 41°25′04″S; 72°16′43″W	200 m	Granitic bands	Zircon	5	0.549 (22)	4.120 (165)	0.428 (5,916)	<1% (<1%)	3.4 ± 0.8			
BR410***	Laguna Patas, Ralún 41°17′17″ S; 72°26′57″W	200 m	Diorite	Zircon	20	3.155 (1,050)	3.663 (1,219)	0.428 (5,916)	9% (21%)	22.4 ± 1.1			
BR411***	L. Llanquihue-Ensenada 41°13′00″S; 72°40′30″W	80 m	Granite	Zircon	7	11.85 (491)	13.81 (572)	0.428 (5,916)	10% (9%)	21.8 ± 1.6			

[a]Analyses by the external detector method using 0.5 for the 4π:2π geometry correction factor. P(χ^2) is the probability of obtaining a χ^2 value for $(v-1)$ degrees of freedom, where v is the number of crystals. *Apatite FT ages calculated using dosimeter glasses CN5 with $\zeta_{CN5} = 333.9 \pm 7.3$ and zircon FT ages using CN2 glasses with $\zeta_{CN2} = 129.9 \pm 1.64$. **Apatite FT ages obtained using dosimeter glasses CN5 with $\zeta_{CN5} = 333.3 \pm 8.2$ and zircon FT ages using CN2 glasses with $\zeta_{CN2} = 130.7 \pm 1.9$. *** Zircon FT ages calculated by M.R.B. using dosimeter glasses CN1 with $\zeta_{CN1} = 119.00 \pm 5.0$

[b]South American Provisory Datum 1956

with respect to orography and to attempt to distinguish in situ post-magmatic cooling from cooling related to uplift and denudation along the LOFZ. 49 samples were obtained during two field seasons to the Main Andean Range in the study area. The Sernageomin office of Puerto Varas provided 11 additional samples from areas of difficult access. Zircons and apatites were analysed using the external detector method (Naeser 1976) and ζ-calibration approach (Hurford and Green 1983; Hurford 1990).

Apatite and zircon crystals were separated, mounted, polished, and etched according to the techniques outlined by Hurford (1990). Apatite mounts were embedded in epoxy, polished, and etched in 5 M HNO_3 for 20 s to reveal tracks. Zircons were mounted in FEP-Teflon, polished, and etched in molten eutectic of NaOH:KOH at 217 ± 4°C using a platinum crucible. Total etching times for zircons varied between 16 and 72 h and were achieved at steps varying between 1 and 4 h, until the majority of the grains were fully etched. The samples were irradiated in the Risø reactor of the National Laboratory at Roskilde, Denmark, or at the Oregon State University TRIGA Reactor, in Corvallis, USA. Zircon packages (RU21, RU22, and RU24) were irradiated with a total thermal neutron fluence of $1.0x10^{15}$ n/cm^2. Apatite packages (RUA20 and RUA21) were irradiated each with a total neutron fluence of $1.2x10^{16}$ n/cm^2. The neutron fluence was monitored using uranium-dosed Corning glasses CN5 for apatite and CN1 or CN2 for zircon. A low-uranium muscovite sheet was used as an external detector to record induced tracks in the minerals and to measure the thermal neutron flux. Fission tracks in the mica detectors of the samples were revealed by etching in 40% HF during 50 min at room temperature. Spontaneous and induced FT densities were counted on a Zeiss Axioplan optical microscope at 1250x magnification. A dry 100x objective for the apatites and an oil-immersion 100x objective was used for the zircons.

ζ_{CN-5} apatite and ζ_{CN-2} zircon values for Adriasola (Table 1) were obtained with the Fish Canyon (apatite and zircon), Durango (apatite), Mount Dromedary (apatite and zircon), Buluk (zircon), and Tardree (zircon) age standards recommended by Hurford (1990). The ζ_{CN-1}–zircon zeta by Brix was applied for samples BR409, BR410, and BR411, and is based on multiple analyses using Fish Canyon, Tardree, Buluk, and Mount Dromedary standards.

Apatite FT lengths were measured using an attached drawing tube and digitizing tablet calibrated against a stage micrometer, following the recommendations of Laslett et al. (1982). Central ages (Galbraith and Laslett 1993) were calculated using the International Union of Geological Sciences (IUGS) recommended ζ-calibration approach of Hurford and Green (1983). A total of 51 apatite and 56 zircon FT ages, plus 37 frequency distributions of confined track-length measurements, are reported in this paper and documented in Table 1.

Fission track results in the Reloncaví area

The location of the samples, the FT ages, and the apatite track-length distributions in the Reloncaví area are plotted in Fig. 5. In general, the apatite FT ages range from early Miocene to Pliocene and tend to be younger towards the LOFZ. Along the fault zone itself, the obtained ages are typically between ~5 and ~3 Ma (the oldest sample along the fault zone is 7.2 ± 2.6 Ma and the youngest 3.3 ± 1.2 Ma).

The mean length and distribution of confined tracks in apatite provide important additional information on the cooling history of rocks below ~120°C (e.g. Gleadow et al. 1986; Green et al. 1989). In general, the measured apatite FT length distributions have long mean track lengths (between 13.6 ± 0.2 and 15.0 ± 0.2 μm) and relatively large standard deviations up to 2.05 μm. The negative-skewness towards shorter tracks indicates that the host rock spent some time in the temperature zone where FTs in apatite are partially annealed (Gleadow et al. 1986). Along the LOFZ, the FT length distributions have all long mean track lengths and tend to narrower deviations (with the exception of sample AA2, Fig. 5), indicating rapid cooling through the apatite partial annealing zone (APAZ, Gleadow et al. 1986).

The distribution of zircon FT ages in the Reloncaví area appears to be concordant with the pattern of intrusion and K-Ar ages from nearby outcrops and therefore tends to mimic the distribution of the outlined plutonic units (Fig. 3). Miocene cooling ages were obtained on the western side of the Reloncaví Estuary and Cretaceous on the eastern shore. Cretaceous ages were also obtained in the eastern part of the study area and along the Lago Todos Los Santos. Late Miocene–Pliocene zircon cooling ages were obtained from samples AA129, AA42, and BR409, which are all located along isolated sectors directly at the trace of the LOFZ, and overlap with the apatite cooling ages within 1σ-error. These are interpreted as reset ages by late magmatism or fluids and are discussed together with other data in the following sections.

Several apatite and zircon FT ages have high age dispersions (> 20%), indicating discordant age distributions (Galbraith and Laslett 1993). High age-dispersions in zircon FT ages from a common source may be produced by differential α-radiation damage affecting individual grains of the sample (e.g. Kasuya and Naeser 1988; Brandon and Vance 1992; Brandon et al. 1998). The metamictisation of zircons, which is mainly produced by radioactive decay of U and Th, apparently shifts their thermal stability towards lower temperature ranges (e.g. Rahn et al. 2004). For apatites, such age variations are commonly due to variations in chemical composition, in particular by the Cl/Fl ratio (e.g. Green 1988; Crowley et al. 1991).

However, in the geological context of an active arc, the scatter in individual grain ages can also result from thermal overprinting by later magmatism or hydrothermal fluids causing differential age resetting of indi-

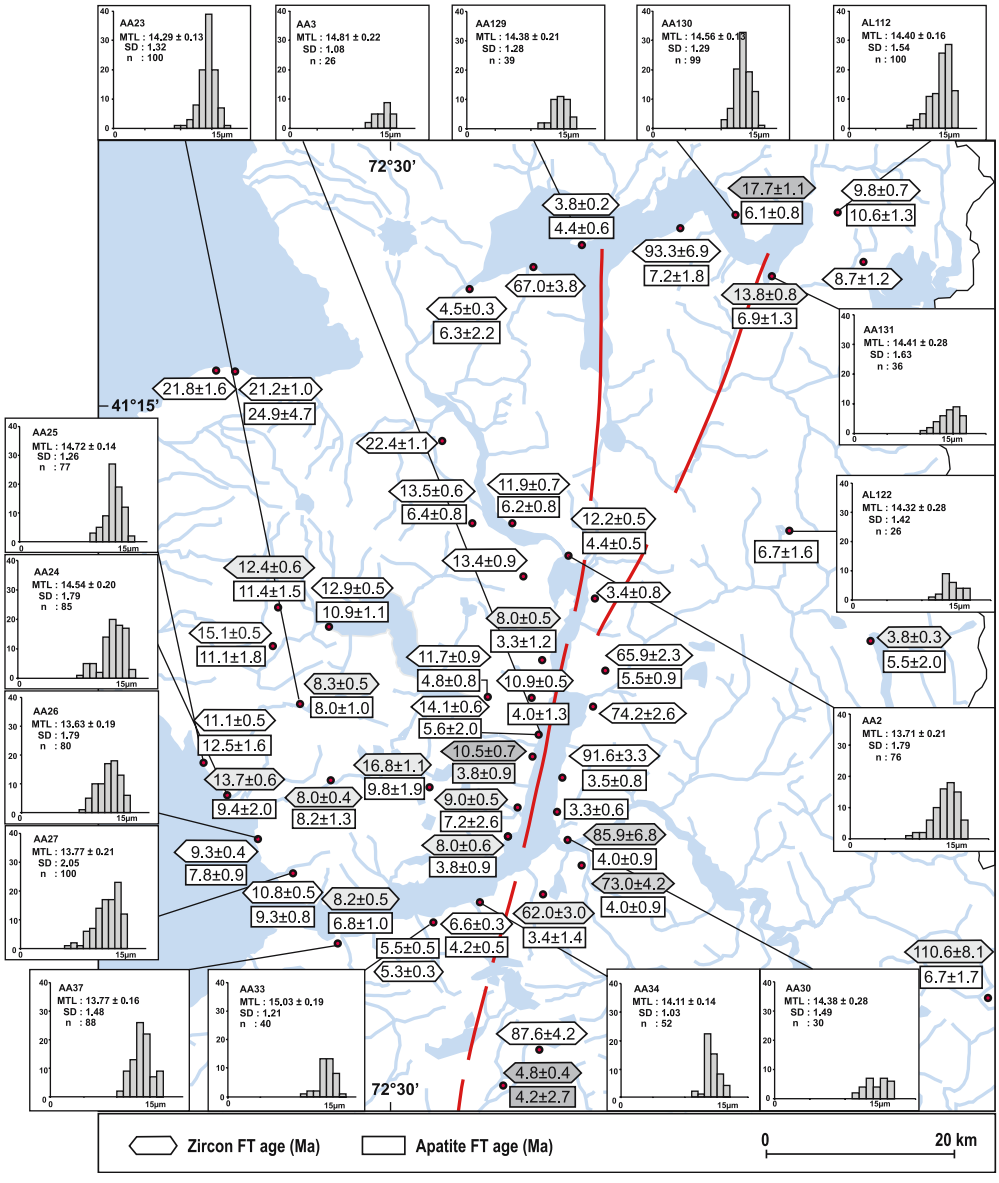

Fig. 5 Zircon and apatite FT ages and confined apatite track-length distributions in the Reloncaví area. Samples with age dispersions > 20% are outlined in *dark grey boxes* and > 10% in *light grey* boxes. Refer to discussion in the text. Apatite track-length histograms (with $n > 25$) with vertical axes representing the number of confined tracks and horizontal axes with the track-lengths binned at intervals of 1 μm. *MTL* mean track length. *n* total number of measured tracks. *SD* standard deviation

vidual grains with different annealing properties (e.g. Thomson et al. 2001; Thomson 2002).

The age dispersion of representative zircon FT grain-ages along the LOFZ is analysed with different plots in Fig. 6. Plots for the variation of the approximate U content of the single grains with respect to their ages show no clear correlation; anomalously older grains are relatively poorer in U concentration with respect to the rest of the grain populations, whereas the younger grains have variable U contents. The radial plots indicate, however, the presence of young Miocene age components accompanied by relative errors below 20%. Why individual zircons from within a single granitoid should show differential partial resetting in response to some thermal event with no apparent correlation to U-content and hence no apparent correlation to accumulated alpha-damage is intriguing. Although variable accumulated alpha-damage in zircon (dominated by the decay path of ^{238}U) is commonly cited as being the third major factor—after temperature and time—affecting the annealing behaviour of FTs in this mineral (e.g. Kasuya and Naeser 1988; Brandon et al. 1998; Rahn et al. 2004), we speculate that the variable annealing seen in this study has some other cause, perhaps related to chemical variation. However, more detailed investigation and discussion of this is beyond the scope of this contribution and merits further study.

In order to identify possible sources of thermal resetting, a classification of age components within the discordant distribution of single FT ages from Cretaceous and Miocene zircon samples was attempted using the program Bonmfit (Brandon 2002).

For Cretaceous samples AA30 and AA31 located near Puelo, their Tertiary component ages are younger than the nearest Ar-Ar ages from similar plutonic units, but older than their apatite cooling ages. These could reflect partial thermal resetting after pre-Tertiary cooling at temperatures below the apatite PAZ, or alternatively thermal resetting by later Miocene shallow intrusions at

the southwestern shore of the Reloncaví Estuary or south of Río Blanco. For sample AA6 at the western shore of the Reloncaví Estuary, with a nearby Early Miocene K-Ar age, and Late Miocene apatite cooling age, late Miocene peaks were identified. This sample is located 5 km north of sample AA4, which has a very rapid cooling history below magmatic temperatures by ~7 Ma. Sample AA130, at the eastern branch of Lago Todos Los Santos, corresponds to an early Cretaceous plutonic unit and is located within 5 km distance range to a plug-shaped stock with an Ar-Ar age of 18.3 Ma.

As a reference, Tagami and Shimada (1996) have shown that zircon FT ages in sandstones surrounding a rapidly cooled granitic intrusion become totally reset within a distance of ~3 km from a steep-dipping contact, although this distance can vary depending on several factors including the size and shape of the intrusives, the permeability of the wallrock, and the presence of fluids (e.g. Kukowski 1992).

Owing to the young ages of the affected apatites and the lack of measurable confined tracks, it was not possible to find any illustrative example for their age variation. The most affected apatite sample in the Reloncaví area, sample AA42, is very young and has a very low spontaneous track density, which in addition severely affected the precision of its central age.

The presence of anomalous copper and base metal mineralisation has been reported in fluvial sediments derived from the intruded metamorphic basement rocks west of the LOFZ (Sernageomin-BRGM 1995). Hydrothermal activity is also present in numerous hot springs along the fault trace; hot springs are found near Ralún, Sotomó, and further south at Pichicolo and on Llancahué Island. Volcanic monogenic cones are also located at the southern end of Estero Cayetué, on the lower slopes of the volcán Osorno and between the Yate and Hornopirén volcanoes.

Despite these considerations, the number of samples with high age-dispersions is nevertheless limited to a minor proportion of the total dated rocks. The overall distribution of zircon and apatite FT ages with respect to the position of the LOFZ still points to the main episode of cooling and denudation along the fault zone being late Miocene–Pliocene in age, affecting rocks at a temperature range between the apatite and zircon PAZ.

FT Results in the Hornopirén area

The distribution of FT ages and track-length data from the Hornopirén area is shown on Fig. 7. Apatite ages are similar across both sides of the fault zone, ranging from 6.5 ± 1.2 Ma to 3.3 ± 0.5 Ma. The corresponding confined track-length distributions have long mean lengths (between 13.7 ± 0.2 μm and 14.9 ± 0.2 μm) and relatively narrow deviations (between 1.5 and 1.3 μm along the fault zone; sample AL181 away from the fault zone had an exceptionally larger deviation of 1.7 μm), pointing out rapid cooling from ~120 to 60°C (Gleadow et al. 1986). Large errors and high age dispersions were obtained in apatite samples AA45, AA106, and AA39 because of the presence of inclusion trails and etched fractures at their grain surfaces. Along both sides of the fault zone, zircon fission-track ages between 6.1 ± 0.5 Ma and 3.2 ± 0.3 Ma overlap the apatite ages within 1σ error. Despite the differences in temperature range of their respective partial annealing zones, the similar apatite and zircon ages imply very rapid post-emplacement cooling rates for the respective intrusives (> 100°C/Myr). High age dispersions obtained in most of the zircon FT samples along the LOFZ are indicative of partial thermal resetting by hydrothermal fluids or magmatic activity in the shallow crust. Sample AA43, taken from an outcrop of dacitic tuff near Pichicolo, yielded overlapping zircon and apatite FT ages of 14.6 ± 0.6 Ma and 15.5 ± 2.7 Ma. These are concordant with an Ar-Ar date obtained from vitric tuffs of an upper member of the Tertiary Ayacara Formation outcropping further south at Huequi (Rojas et al. 1994). This sample is interpreted as the extrusion age of the volcanic unit and is discarded for the tectonic and cooling history of the area.

Discussion: cooling history of the North Patagonian Batholith and late Cenozoic denudation

Numerical simulations of the ascent and emplacement of granitic intrusives reveal that viscosity contrasts and absolute viscosity of magmas determine the splitting behaviour and differing emplacement levels of magma chambers (Kukowski and Neugebauer 1990; Kukowski 1992). According to these simulations, ascent and emplacement typically occur within less than 1 Myr. The cooling histories of the intrusive bodies depend on their volume, shape, and level of emplacement. Within the upper ~15 km of the crust, thermal channels (with temperatures exceeding 900°C) in the magmatic systems can be established over time spans of up to ~2 Myr, allowing for splitting of magma chambers with contrasting densities and emplacement at different levels. At shallow levels in the upper crust (~5 km), heat transfer from a magma chamber is likely to occur through convection of hydrothermal fluids. Depending on the permeability of the wallrock, the anomalous heat flow affects the shape and distribution of the geothermal gradients in their surroundings, lifting the isotherms in the area above the chamber towards the Earth's surface. Furthermore, if the base of the chamber is connected through channels with a reservoir of hot magma, the thermal perturbation and fluid circulation may persist for several millions years (Marsh 2000; Best 2003).

Thermal constraints for the interpretation of T-t histories for the NPB

The interpretation of thermochronologic data usually invokes the closure temperature concept (Dodson 1973),

i.e. the temperature for a given system at the time represented by its apparent age. For each system, the closure temperature is a function of the cooling rate, mineral composition, damage structure, and other specific properties that are still not completely understood (e.g. Harrison et al. 1985). A precondition for integrating FT ages with normal isotopic systems to learn about the low temperature part of cooling paths is that the studied samples have not undergone any complex thermal history at low temperatures (e.g. Dokka et al. 1986). In the present study, this assumption is often supported by the FT track-length distributions of the apatites. High age dispersions, however, may result in some places from thermal overprinting causing differential resetting of zircons with different characteristics by nearby intrusions or fluid activity. Cretaceous plutons with high dispersions in their cooling ages may point out a history of earlier exhumation, followed by reburial and a second later phase of exhumation (e.g. Thomson et al. 2001). This latter scenario is, however, unlikely in the study area considering the low P contact metamorphic aureoles in the intruded wallrocks and the little amount of Cenozoic overburden exposed in the Main Range. Miocene zircon FT ages with high age dispersions could represent thermal perturbations during the cooling histories of plutons, affecting the T-t paths of rocks exposed along the fault zone. U-Pb zircon and whole-rock Rb-Sr ages are assumed to yield the time of magmatic intrusion (e.g. Faure 1986). Amphibole K-Ar and Ar-Ar closure temperatures record closure in a ''transition zone'' at 500 ± 50°C (Harrison 1981). Closure temperatures of 350 ± 50°C and 300 ± 50°C have been assumed for the low temperature magmatic and/or metamorphic cooling K-Ar and Ar-Ar ages of muscovite and biotite, respectively (Purdy and Jäger 1976; Stöckhert et al. 1999). Assuming rapid or monotonic cooling rates exceeding 5°C/Myr, extrapolated closure temperatures for the zircon and apatite FT systems were set at 280 ± 30°C and 100 ± 20°C, respectively (Wagner and Reimer 1972; Hurford 1986; Wagner et al. 1994; Brix et al. 2002; Thomson 2002). Where available, T-t paths for the apatite FT system were constructed using inverse modelling based on the well-known annealing characteristics of the Durango apatite (Laslett et al. 1987). Modelling was carried out with the software AFTSolve (Ketcham et al. 2000). The interpretation of the T-t paths for this study focussed mainly on the magmatic cooling processes.

Interpretation of different T-t Histories for the plutons of the NPB

54 cooling paths for the plutonic rocks of the NPB were constructed by correlating the available thermochronologic data of the region with the FT ages obtained in this study. Because the correlation was established between samples dated with different geochronologic methods, and taken during different field seasons, we regard these with a generalised interpretation based on different types of intrusions. Samples AA125, BR410, and AL106 were excluded from the interpretation because of the lack of thermochronometers for the correlation. Cooling histories for samples AA8, AA10, AA128, AL143, BR409 and BR411 were interpolated with data from nearby samples with complete thermal information. The shapes of the derived T-t plots allowed classification of the cooling histories into three main types (Fig. 8a):

Type A paths describe very slow cooling rates after initial rapid postmagmatic cooling following emplacement at depths of ~7–10 km in Cretaceous times and rapid unroofing in the late Cenozoic. We envision that the sampled pluton experienced slow, conductive cooling at depth. This type of cooling corresponds well to predictions for plutons with large surface-to-volume ratios (Kukowski 1992; Best 2003). For type A, the cooling rate has a downwards-concave shape between ~100 and ~30 Ma, is generally less than 2.5°C/Myr at temperatures below ~300°C and increases progressively from ~30 to ~5 Ma. Along the LOFZ, most of these rocks cooled rapidly below the APAZ (~50°C/Myr below 150°C) in the late Miocene-Pliocene, as shown by the Durango apatite models from AFTSolve. However, the wide time-span given in the correlation between different thermochronometers allows two possibilities: either the plutons remained at near-constant depths during most of the Cenozoic until exhumation in the late Miocene (type A1), or alternatively, they were previously denuded and reburied or re-heated sufficiently to totally reset the apatite FT system (type A2; e.g. Thomson et al. 2001). This latter scenario may be likely for samples AA30, AA31, and AA130, which display partially reset zircon FT ages (Fig. 6). The curves are based on the correlation of zircon and apatite FT ages with mid-Cretaceous biotite K-Ar and Ar-Ar cooling ages from the Reloncaví area (Carrasco 1995; Sernageomin-BRGM 1995). Al-in-Hornblende geobarometry by Seifert et al. (2003) support the inferred emplacement depths for these intrusives.

Type B paths describe moderate and steady cooling rates following deep emplacement at some time between Cretaceous and early Miocene. For type B, the rates range between ~20°C/Myr and 50°C/Myr. The steady cooling rates suggest that the plutons were exhumed from emplacement depths exceeding 10 km. This inference is in agreement with depths of emplacement determined with Al-in hornblende geobarometry data from plutons along the LOFZ by Seifert et al. (2003). With the exception of one early Miocene Rb-Sr date by Munizaga et al. (1988), no intrusion dates are available for these plutons. We interpret these cooling rates to correspond to deep magma chambers split along the LOFZ near their emplacement level (e.g. Kukowski 1992).

Type C paths indicate very rapid cooling after emplacement in the Miocene and Pliocene at shallow levels in the upper crust, e.g. at less than ~5 km depth. Cooling rates well exceed 50°C/Myr and are comparable

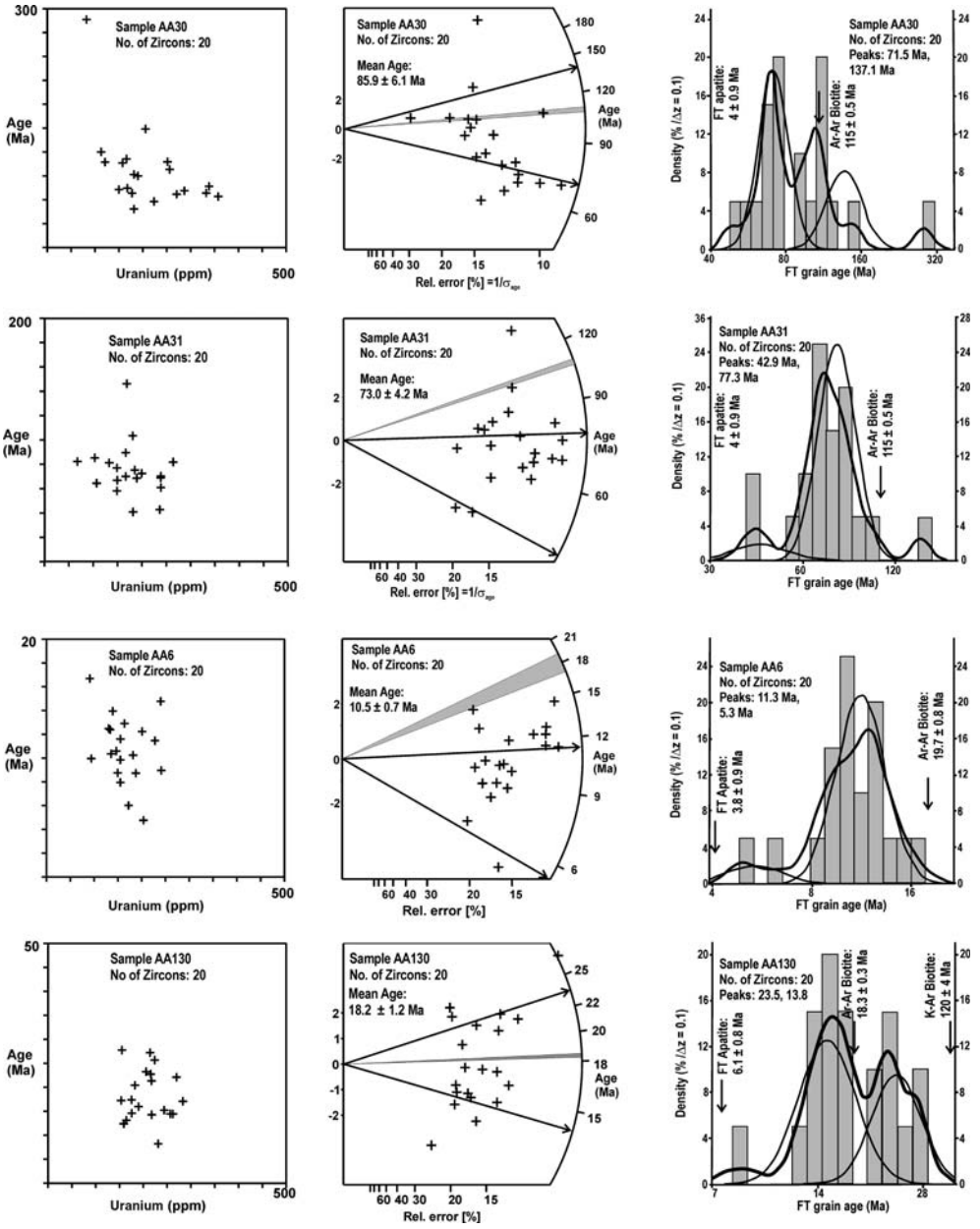

Fig. 6 U-Age plots, radial plots (Galbraith 1990), and probability density distribution plots with best-fit peaks determined from Binomfit (Brandon 2002) for selected zircon FT ages with high age dispersions along the LOFZ in the Reloncaví area. The *thick line* is the probability density distribution. The *thin lines* show the component distributions estimated by the binomial peak-fit method of Brandon (1996). The *arrows* in the radial plots correspond to the best-fit peak ages for the sample. The *gray bars* in the radial plots are the Ar-Ar biotite dates from the nearest outcrops of the same plutonic unit. The younger age components suggest partial resetting by later magmatic or hydrothermal activity, refer to discussion in text

to those described at deformation zones in core-complex settings (e.g. Johnson et al. 1997). Here, such high cooling rates are unlikely to correlate with tectonic activity and rapid erosion along the magmatic arc of the subduction zone, but instead should reflect cooling related to heat transfer through hydrothermal fluid convection atop a magmatic body close to the surface (Kukowski 1992).

The regional distribution of the cooling path types within the rocks of the NPB is shown in Fig. 8b. Type A cooling paths are concentrated along the eastern border of the Reloncaví Estuary and scattered across the Todos Los Santos Lake and at the eastern side of the Main Range. Type B paths were obtained for plutons at the western shoreline of the Reloncaví Estuary and at the eastern border of the Todos Los Santos Lake. The relative alignment of the types A and B cooling paths with respect to the position of the main fault strand of the LOFZ along the Reloncaví Estuary indicates a western-side uplift between plutons emplaced at different levels and different times. The relative movements must have ended in the Pliocene (~5–3 Ma), given by the similar ages indicated by the steep cooling curves below the apatite PAZ on both sides of the fault zone. A similar comparison between the different T-t histories at the eastern border of the Todos Los Santos Lake indicates an eastern-side uplift across the NNE-trending fault segment of the LOFZ.

Type C cooling paths are irregularly distributed on the Main Range and along isolated sectors of the LOFZ, resembling plutons emplaced over deeper units of the NPB. For display on the maps, their ages of

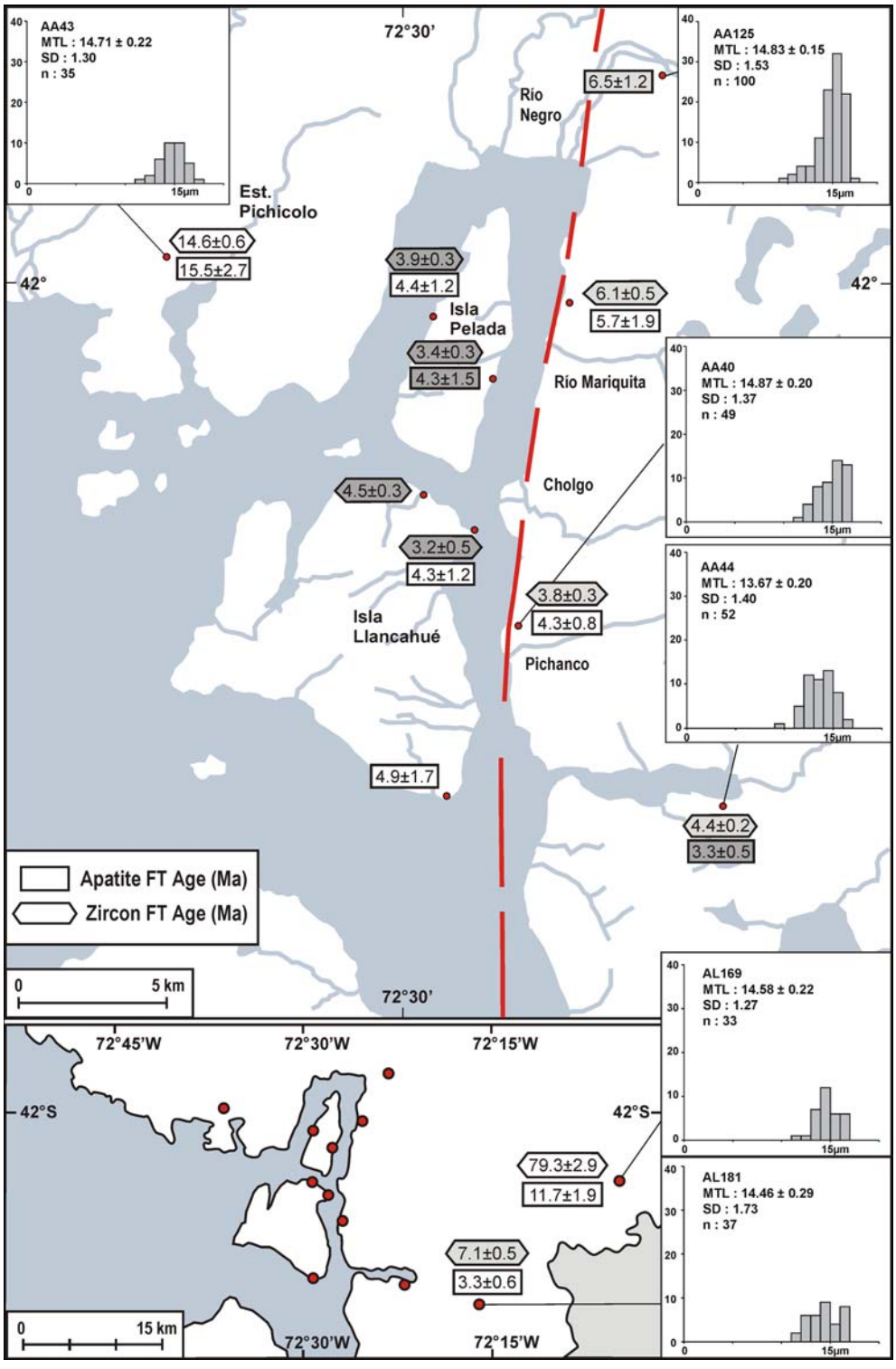

Fig. 7 Zircon and apatite FT ages and confined apatite track-length distributions in the Hornopirén area. Grey boxes indicate samples with high age dispersions (see legend in Fig. 5). Refer to text

intrusion were binned at intervals of 15 ± 2.5 Ma, 10 ± 2.5 Ma, 5 ± 2.5 Ma. This classification reveals a tendency of younger ages towards the LOFZ. In the Hornopirén area, type C T-t curves are located on both sides of the LOFZ. Additionally, these fast cooling rates imply that the intruded wallrocks must have been at low temperatures. This is consistent with the low-pressure contact metamorphic aureoles in the basement rocks on Llancahué Island (Pankhurst et al. 1992). The partially reset zircon FT ages obtained along the fault zone can thus be interpreted as representing older wallrocks reheated to temperatures of partial annealing of FTs in zircon by the later shallow intrusions in the area.

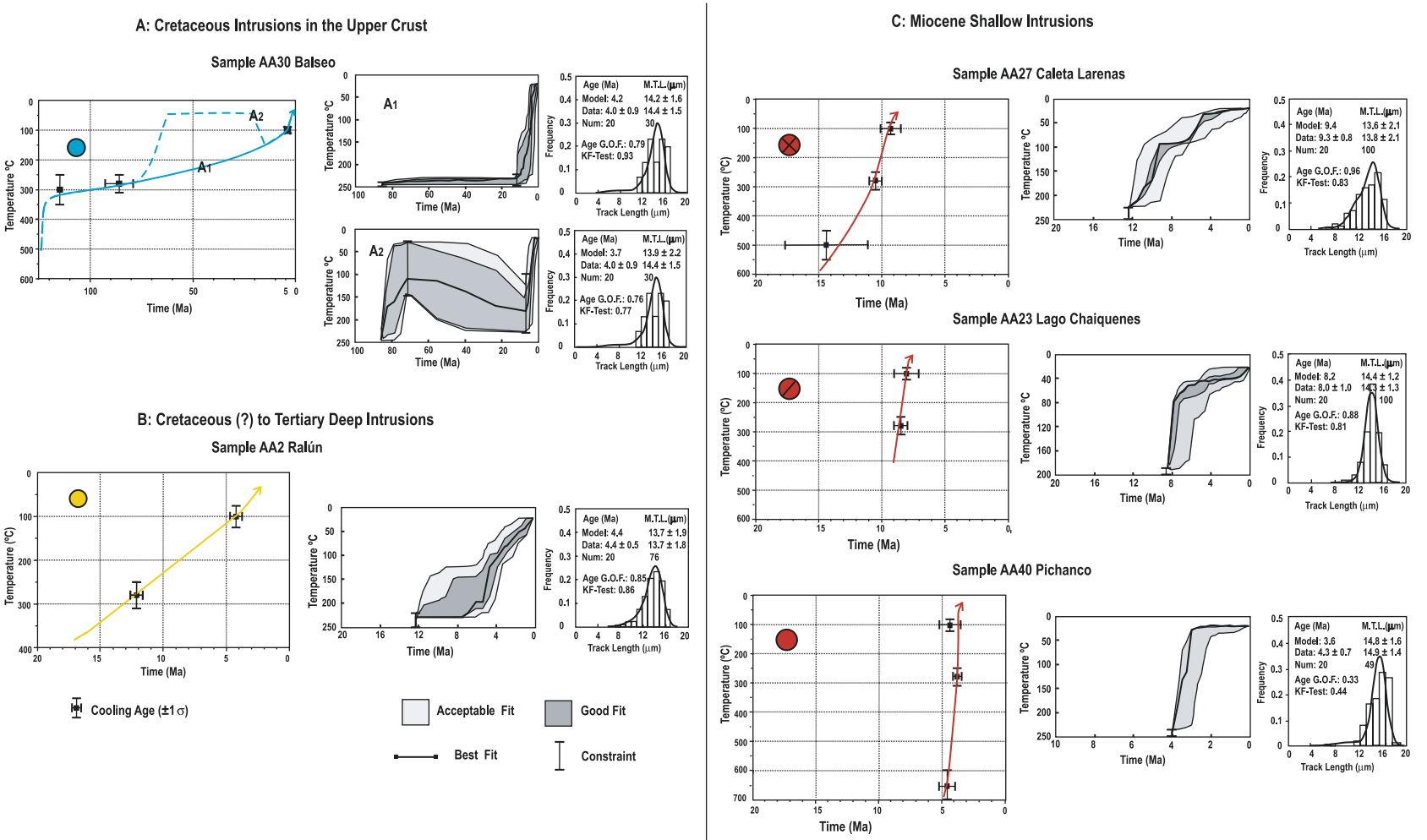

Fig. 8 **a** Examples of different temperature vs. time (T-t) histories obtained from different plutons of the North Patagonian Batholith in the study area. *Coloured symbols* are used for the regional classification in **b**. *Left:* diagrams and cooling paths are based on closure temperatures of different thermochronometers. *Right:* results of thermochronologic modelling based on the Durango apatite model (Laslett et al. 1987) and an initial track length of 15.7 µm. The low T-t histories are displayed at the centre. Three different reliability levels (best fit = *black line*, good fit = *dark grey* envelope, accepted fit = *light grey* envelope) describe the modelled results with envelopes and a curve at the centre. Independent geologic constraints are indicated with vertical brackets. At the *right side*, the results are displayed as a frequency distribution of measured confined track length data overlain by a calculated probability density function (best fit). *Model*: modelled FT-age and mean track length. *Data*: measured weighted mean FT-ages and confined track lengths. *Num*: number of single grains and measured track lengths. *G.O.F.*: Goodness of fit. *KF*: Kolmogorov–Smirnov test. The samples are classified in terms of the shape of the curves. For type A plutons, two different constraints for their T-t histories (A_1 and A_2) are displayed, allowing the possibility of exhumation in Pre-Tertiary times. **b** Distribution of the T-t histories of the plutons of the North Patagonian Batholith in the Reloncaví and Hornopirén areas of the Main Range. *LOFZ*: Liquiñe-Ofqui fault zone. *CVG*: Central Valley Graben

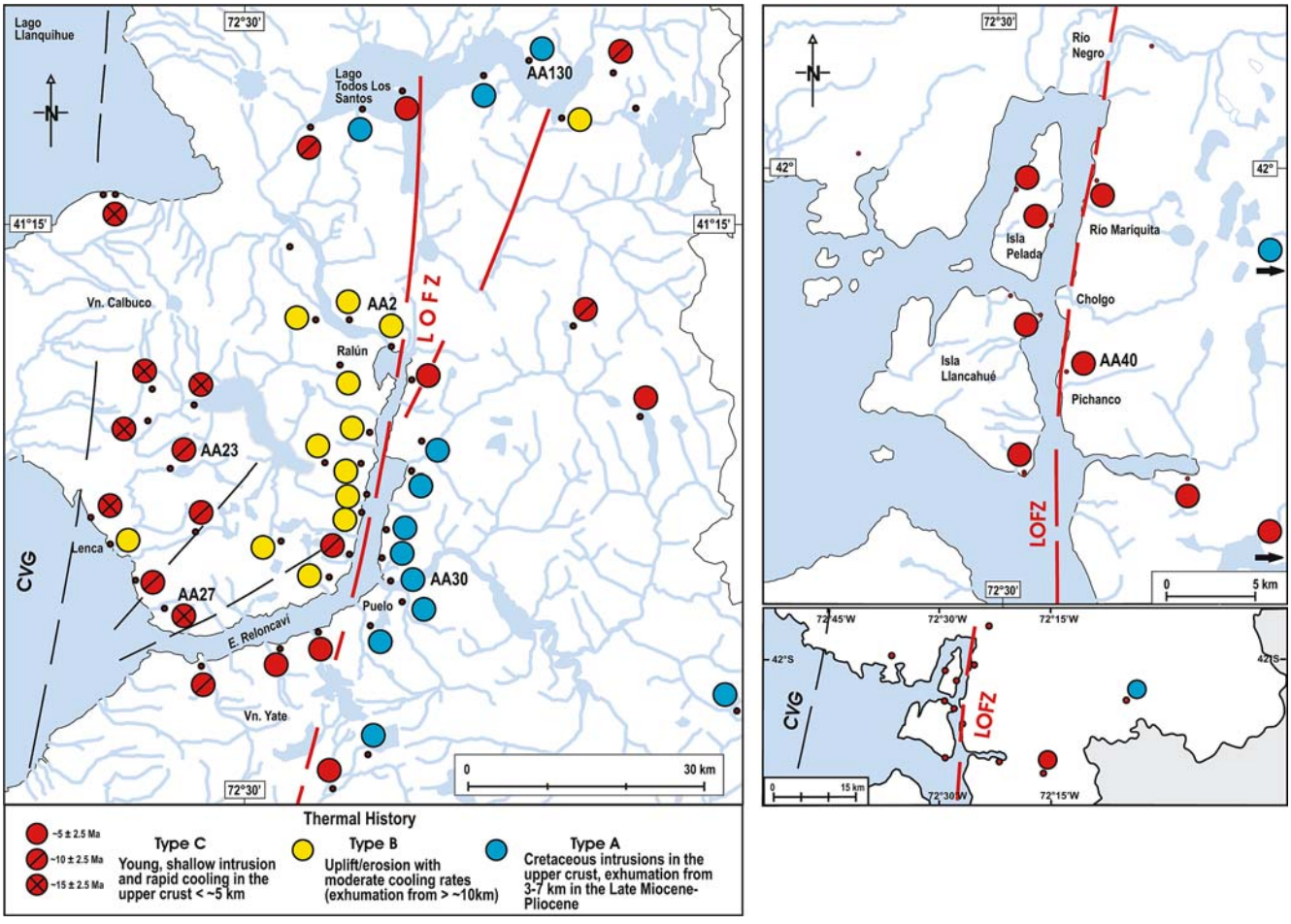

Fig. 8 (Contd.)

Timing and nature of denudation along the LOFZ

If the episode of differential denudation is controlled by vertical displacement along the LOFZ, then this movement can be dated as late Miocene. The timing of cessation of relative vertical displacement is constrained by the steep curves in the apatite FT cooling histories along the fault zone, which imply uniform fast cooling and hence denudation since ~6 Ma (Figs. 5, 7, 8a, b). The most likely cause of this denudation is preferential erosion of transpression-driven uplifted fault blocks. Ramos and Kay (1992) infer a transpressional tectonic configuration for the Southern Andes during the late Miocene. Plate tectonic reconstructions show that the Chile Rise was subducted beneath the Taitao Peninsula between ~7 and ~4 Ma (assuming that the ridge was subducted with a constant rate of 2 cm/year since ~10 Ma, e.g. Cande and Leslie 1986; Ramos and Kay 1992; Thomson et al. 2001). Strain partitioning in the overriding plate is suggested from the different structural domains along the Andean orogen to the north and south of the CTJ (Dewey and Lamb 1992; Diriason et al. 1998; Lavenu and Cembrano 1999). North of the CTJ, a significant amount of contraction in the arc region appears to have been taken up by transpression along the right-lateral LOFZ in late Cenozoic times (Thomson 2002). In contrast, estimates for total horizontal shortening of the back arc between latitudes 47°S and 42°S amount to ~8 km, less than a third of the amount of contraction observed south of the Triple Junction and north of ~37°S (Diriason et al. 1998; Vietor and Echtler 2005). However, evidence for earlier transpression along the LOFZ is limited. This is probably because of its long-lived history, active since Cretaceous times, and because episodic magmatism along its traces has overprinted previous deformation (Cembrano et al. 1996; Adriasola 2003).

Amounts of Denudation along the LOFZ

Constraints on the amounts of denudation along the LOFZ are difficult to obtain. Apart from tectonic forcing, denudation, particularly erosion, may be driven by other processes, like the steepening of local relief (rather than an increase in elevation), changing climate, and orography (e.g. Whipple et al. 1999; Fitzgerald et al. 1995; Small 1999; Montgomery et al. 2001; Montgomery

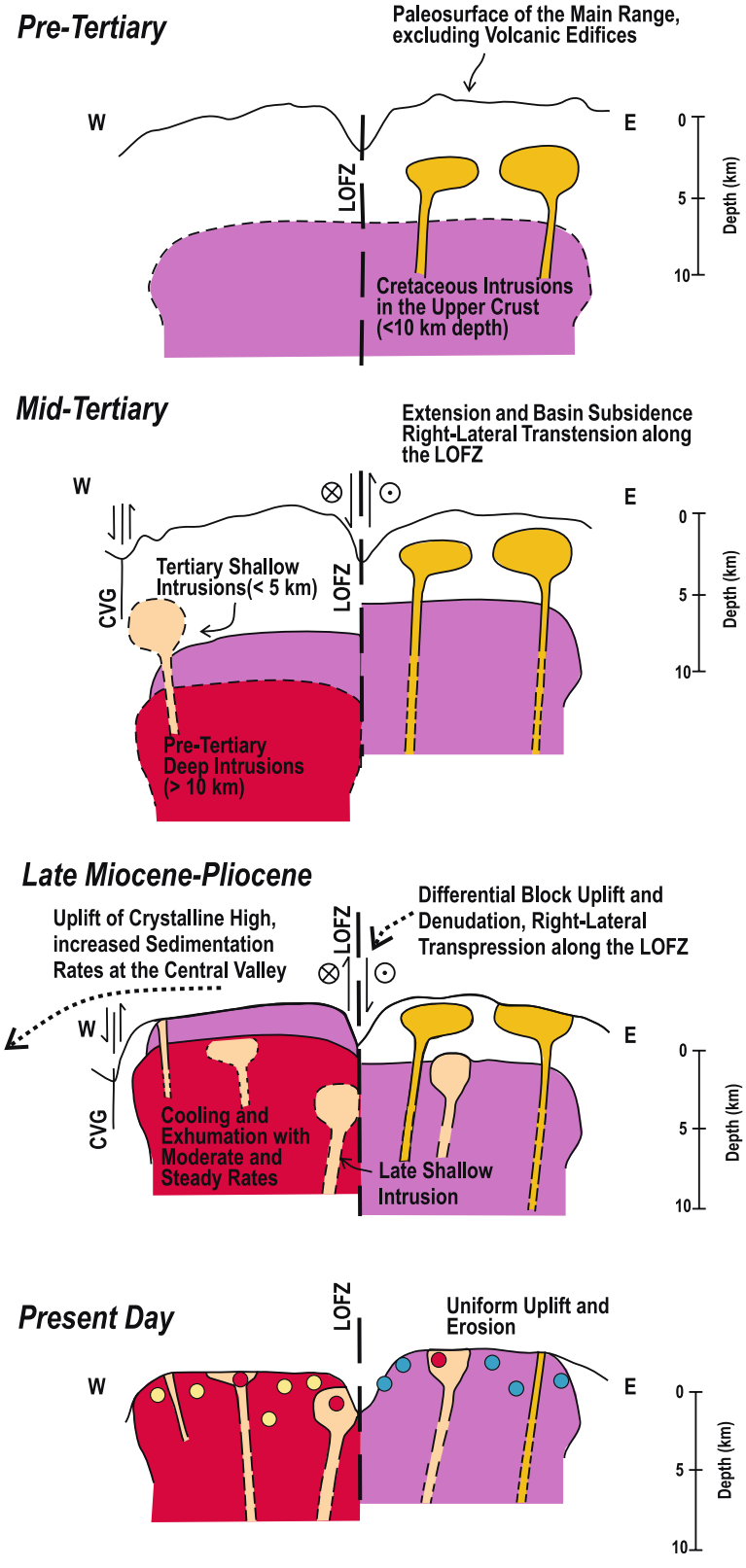

Fig. 9 Scheme of the tectonic evolution of the North Patagonian Batholith in the Los Lagos-Chiloé Regions along the Liquiñe-Ofqui fault zone (LOFZ) inferred from their T-t histories in this study. Partially crystallised plutons are outlined in dashed lines. *CVG*: Central Valley Graben. *Uppermost line* represents the topography of the Main Range excluding the volcanic edifices

and Brandon 2002; Willet 1999). The translation of cooling histories derived from thermochronology to denudation rates requires knowledge of the upper crustal geothermal gradient, which in this region is likely to vary in time as a function of magmatic heat input, topography, heat advection, and convective circulation in the upper crust (e.g. Kukowski 1992; Mancktelow and Grasemann 1997). Regional surface heat flow measure-

ments yield current values of ~80–100 mW/m^2 (Hamza and Muñoz 1996; Muñoz 1999). Thermal conductivities for granitoids vary between 2.5 and 3.5 W/(m·K) (Seipold 1998). Thus, present-day geothermal gradients of 32 ± 8°C/km can be estimated for the upper crust. A reasonable denudation estimate along the LOFZ can be obtained from the uplifted blocks represented by plutons with type B T-t histories, exhumed with moderate and steady cooling rates from depths exceeding 10 km. These were well identified on the western shore of the Reloncaví Estuary. Their cooling curves describe rates of ~20 to 30°C/Myr from 12 to 8 Ma at temperatures below 300°C, followed by increased rates at temperatures below the apatite PAZ in the Late Miocene–Pliocene (Figs. 8a, b). Assuming that the present-day geotherm has remained constant since the late Cenozoic stage of denudation, their average cooling rates of ~30 to 50°C/Myr would imply denudation rates of ~0.9 mm/year to 1.6 mm/year (or between 0.8 and 2.2 mm/year for constant geotherms derived from surface heat flow values between 80 mW/m^2 and 100 mW/m^2). Supposing an early Miocene intrusion age of ~20 Ma for these plutons, the average post-emplacement exhumation rates constrained with Al-in-hornblende geobarometry would be below ~1 mm/yr. Denudation rates determined from thermochronology may be overestimated due to the effect of topography or the advection of isotherms, as they rely on cooling rates of samples located at the bottom of a valley. For a comparable sinuous topography with a wavelength of ~20 km, an amplitude of ~1.5 km, a geotherm of 20°C/km, and steady-state erosion rates of ~1–2 mm/year, Stüwe et al. (1994) calculated that the topographic effect would lead to an overestimation by ca. 20%. Direct conversion of cooling rates to exhumation rates that assume a simple constant linear geotherm can markedly underestimate peak exhumation rates where exhumation rates are rapid (>1 to 2 mm/year), and overestimate rates during periods of isotherm relaxation when exhumation wanes (Mancktelow and Grasemann 1997). Furthermore, as the regional landscape is severely affected by Plio-Pleistocene glaciation, it is difficult to judge how the present day topography has been modified after the samples cooled through the FT closure temperature isotherm. For mountain belts that intersect the snowline, glacial erosion processes operating above the mean glacial equilibrium-line-altitude (ELA) appear to place an upper bound to the stability of topography, above which only a small volume of uplifted rock survives erosion at a geologic timescale (Brozovic et al. 1997). The modal elevation of the modern perennial snowline in the region, a proxy for the regional ELA, varies between 1,500 and 2,000 m above sea level, and lies typically ~1–1.5 km beneath the mountain summits (Montgomery et al. 2001). A dissected Pleistocene ice-capped volcano, Monte Tronador (41°09′S, 71°53′W; 3,470 m above sea level) represents the highest elevation of the region. As a reference, Thomson (2002) compared glacial erosion rates in Patagonia with estimations by Hallet et al. (1996) for high ice-flux, temperate-glacier landscapes in Alaska, which vary between 10 and 100 mm/year, and clearly exceed denudation rates estimated by FT thermochronology.

At present, climate in Patagonia is controlled by persistent winds with a westerly component (so-called westerlies) driving storms against the western flanks of the southern Andes, and locally precipitation rates exceed 4,000 mm/year (New et al. 2002). These rates are comparable in magnitude with the Monsoon precipitation rates at the foothills of the Greater Himalayas, where bedrock river-incision has been shown to be a very effective erosion agent keeping pace with the development of topography (e.g. Burbank et al. 1996, 2003). However, the much lower mean glacial ELA throughout much of the Plio-Pleistocene in Patagonia, as compared to the Himalaya, means that the precipitation in Patagonia is dominated at relatively low elevations by snowfall, leading to a landscape that has clearly been dominated by glacial erosion, rather than fluvial erosion processes, during the Plio-Pleistocene.

At Hornopirén, the presence of very young and shallow intrusions hampers any direct estimate of denudation rates. Al-in-Hornblende geobarometry indicates a maximum crystallisation depth of ~15 km (0.5 GPa) for the deformed tonalites of the uplifted eastern block of the LOFZ (Seifert et al. 2003; Hervé et al. 1996). Combined with an intrusion age of 9.9 ± 0.2 Ma (Cembrano et al. 2000), an average denudation rate of ~1.5 mm/year since the time of emplacement can be inferred. The apatite FT ages from the Hornopirén area are nevertheless similar to those obtained along the LOFZ at Reloncaví and therefore may correspond to the regional pattern of denudation outlined in this study, which was active between ~5 to 3 Ma. In this context, if the apatite FT ages along the eastern border of the fault zone indicate denudation dates, this would imply a maximum rate of ~3 mm/year after emplacement (albeit for a limited duration).

Regional implications

The above-mentioned rates should be regarded as upper bounds for total denudation rates in the region, as they represent uplifted blocks oppositely distributed along the fault zone. As a consequence of differential exhumation, intrusions with different timing and level of emplacement within the NPB are exposed on both sides of the LOFZ. The late shallow intrusions may have been emplaced into dilational zones created during right-lateral movements along the fault zone, as described along shear zones within magmatic arcs by Paterson et al. (1991), Hutton and Reavy (1992), and Tikoff and Saint Blanquat (1997).

The results of this study support the assumption of a coupling between magmatism and late Cenozoic tectonics along the southern Andes. The widespread exposure of the NPB along the Main Range, its relatively low and homogeneous topography, and the poor

preservation of Meso-Cenozoic cover sequences can be attributed to intense erosion produced by Plio-Pleistocene glaciation (e.g. Montgomery et al. 2001; Thomson 2002) and local fluvial incision at lower elevations and lower latitudes (e.g. Burbank et al. 1996, 2003). Independent evidence for significant amounts of Cenozoic erosional denudation is provided by the local presence of a ~4-km-deep intramontane basin revealed by oil well data and a seismic reflection profile across the Ancud Gulf at 42°S (Fig. 1). This basin forms part of a discontinuous system along the Central Valley and is bounded to the north by a basement high represented by the uplifted crystalline block at Reloncaví (Gonzalez 1989). The infill consists of more than 3 km of Eocene to Miocene continental and marine clastic sedimentary and volcaniclastic rocks lying unconformably over the basement. Plio-Pleistocene glacial deposits, more than 1 km thick, intercalated with basaltic lava have been reported at the top of this sequence. This indicates that sedimentation input rates during the Tertiary (for a period of 30 Myr) were increased in the past 5 Myr by a factor of 2.

A sketch of the tectonic evolution of the different types of plutons of the NPB in the Reloncaví area is shown in Fig. 9. Cretaceous plutons resemble the oldest remnants of the arc in the past, where the LOFZ began its activity as a thermally weakened zone in the lithosphere above the mantle wedge. The formation and subsidence of the Central Valley in the early to mid Tertiary was accompanied by dextral and normal displacements of the LOFZ along the Main Range. In this context, shallow intrusions were emplaced favoured by deep structures. In the Late Miocene, exhumation of deeper intrusions occurred in a regional denudation episode probably coeval with the northward migration of subducted transform fault segments of the Chile Rise beneath the arc at the latitude of Golfo de Penas. Tectonic unroofing was accompanied by late, shallow magmatism along the LOFZ. Erosion was enhanced by Plio-Pleistocene glaciation and intense precipitation resulting in the development of an upper bound to the topography and mean elevation of the Main Range.

Conclusions

The application of zircon and apatite FT thermochronology along the NPB between 41°S and 42°15′S, combined with a compilation of available geochronologic and geobarometric data from the region, allows the following conclusions:

1. Three different classes of intrusions building the NPB can be distinguished by their T-t histories and geographic distribution:
   (a) Cretaceous intrusions emplaced in the upper 10 km of the crust, with an initial stage of rapid cooling after emplacement and subsequent very slow cooling rates at lower temperatures. Along the LOFZ, these were rapidly exhumed in the late Miocene–Pliocene.
   (b) Cretaceous (?) to Miocene deep intrusions exhumed along the LOFZ with moderate and steady cooling rates from depths exceeding 10 km.
   (c) Tertiary shallow intrusions, characterised by very rapid cooling after emplacement in the upper 5 km of the crust. The very rapid cooling probably resulted from convection of hydrothermal fluids.
2. Apatite FT thermochronology indicates that the LOFZ was the focus of enhanced cooling and denudation between ~5 and 3 Ma. If the preceding episode of differential denudation is related to variable vertical components along the fault zone, then this period of movement can be dated as late Miocene. The most likely cause for denudation is right-lateral transpression, in agreement with the geodynamic situation of the southern Andes north of the CTJ. The dated movement along the LOFZ is coeval with plate tectonic reconstructions for the arrival and subduction of the Chile Rise beneath the Taitao Peninsula.
3. Transpression along the LOFZ was probably coupled with magmatic activity. Direct estimates for the amounts of denudation are thus complicated by possible time-variations of the geotherm in response to magmatic heat input, topography, and convective fluid circulation in the upper crust. Differential exhumation rates of ~1 to 2 mm/year (for a time span of about 5–3 Ma) are considered upper bounds for denudation rates in this part of the Andean region.

Acknowledgements A.C. Adriasola was sponsored by DAAD Grant A/99/02931. Field work was funded by DFG Grant Sto 196/11-2 and by Fondecyt Grant 1980741 to F. Hervé from the Universidad de Chile. We thank especially Jorge Muñoz and Sernageomin - Puerto Varas for their logistic help at field and for providing additional samples for FT dating. We thank C. Mpodozis from ENAP for his valuable comments concerning the regional geology of the study area. Frank Hansen and Ralf Kloke are thanked for preparing the mineral separates. The paper benefited greatly from very constructive reviews by M. Rahn and E. Hejl.

References

Adriasola AC (2003) Low temperature thermal history and denudation along the Liquiñe-Ofqui fault zone in the Southern Chilean Andes, 41–42°S. PhD Thesis, Ruhr-Universität Bochum, 119 pp. URN: urn:nbn:de:hbz:294–11509

Beck ME, Rojas C, Cembrano J (1993) On the nature of buttressing in margin-parallel strike-slip fault systems. Geology 21:755–758

Beck ME, Burmester R, Cembrano J, Drake R, García A, Hervé F, Munizaga F (2000) Paleomagnetism of the North Patagonian Batholith, southern Chile. An exercise in shape analysis. Tectonophysics 326:185–202

Best MG (2003) Igneous and metamorphic petrology, 2nd edn. Blackwell Science, United Kingdom, p 756
Brandon MT (1996) Probability density plot for fission-track grain-age distributions. Radiat Meas 26:663–676
Brandon MT (2002) Decomposition of mixed grain age distributions using Binomfit. On Track 24:13–18
Brandon MT, Vance JA (1992) New statistical methods for analysis of fission-track grain-age distributions with applications to detrital zircon ages from the Olympic subduction complex, Western Washington State. Am J Sci 2:565–636
Brandon MT, Roden-Tice MK, Garver J (1998) Late Cenozoic exhumation of the Cascadia accretionary wedge in the Olympic Mountains, northwest Washington State. Geol Soc Am Bull 110:985–1009
Brix MR, Stöckhert B, Seidel E, Theye T, Thomson SN, Küster M (2002) Thermobarometric data from a fossil zircon partial annealing zone in high pressure-low temperature rocks of eastern and central Crete, Greece. Tectonophysics 326:185–202
Brozovic N, Burbank DW, Meigs AJ (1997) Climatic limits on landscape development in the northwestern Himalaya. Science 276:571–574
Burbank DW, Leland J, Fielding E, Anderson RS, Brozovic N, Reid MR, Duncan C (1996) Bedrock incision, rock uplift and threshold hillslopes in the northwestern Himalaya. Nature 379:505–510
Burbank DW, Blythe AE, Putkonen B, Gabet E, Oskin M, Barros A, Ojha TP (2003) Decoupling of erosion in the Himalayas. Nature 426:652–655
Cande SC, Leslie RB (1986) Late Cenozoic tectonics of the southern Chile trench. J Geophys Res 91:471–496
Carrasco V (1995) Geología y geoquímica del Batolito Norpatagónico y rocas volcánicas asociadas a la zona de falla Liquiñe-Ofqui (41°−05-41°40'LS), X región. Mem de Titulo Depto Geol Univ de Chile, Santiago, Chile, p 127
Cembrano J, Hervé F, Lavenu A (1996) The Liquiñe-Ofqui Fault Zone: a long lived intra arc fault system in southern Chile. Tectonophysics 259:55–66
Cembrano J, Schermer E, Lavenu A, Sanhueza A (2000) Contrasting nature of deformation along an intra-arc shear zone, The Liquiñe-Ofqui Fault Zone, Southern Chilean Andes. Tectonophysics 319:129–149
Cembrano J, Lavenu A, Reynolds P, Arancibia G, Lopez G, Sanhueza A (2002) Late Cenozoic transpressional ductile deformation north of the Nazca-South America-Antarctica triple junction. Tectonophysics 354:289–314
Crowley KD, Cameron M, Schaefer RL (1991) Experimental studies of annealing of etched fission tracks in fluorapatite. Geochim Cosmochim Acta 55:1449–1465
De la Cruz R, Suárez M, Covacevich V, Quiroz D (1996) Estratigrafía de la zona de Palena y Futaleufú (43°15'- 43°45' LS), X Region, Chile XIII Congreso Geológico Argentino y III Congreso de Exploración de Hidrocarburos. Actas 1:417–424
Dell'Angelo LN, Tullis J (1989) Fabric development in experimentally sheared quartzites. Tectonophysics 169:1–21
Dewey JF, Lamb SH (1992) Active tectonics of the Andes. Tectonophysics 205:79–95
Diriason M, Cobbold PR, Rosello EA, Amos AJ (1998) Neogene dextral transpression due to oblique convergence across the Andes of northwestern Patagonia, Argentina. J South Am Earth Sci 11:519–532
Dodson MH (1973) Closure temperature in cooling geochronological and petrological systems. Contrib Mineral Petrol 40:259–274
Dokka RK, Mahaffie MJ, Snoke AW (1986) Thermochronologic evidence of a major tectonic denudation associated with detachment faulting, northern Ruby Mountains-East Humboldt Range, Nevada. Tectonics 5:995–1006
Duhart P, Crignola G, Ordoñez BA, Muñoz J (2000) Franjas metalogénicas en Chiloé continental (41°−44°S) IX Congreso Geológico Chileno, Puerto Varas, Chile. Actas 1:201–205
Faure G (1986) Principles on Isotopic Geology. John Wiley, New York pp 589
Fitzgerald PG, Sorkhabi RB, Redfield TF, Stump E (1995) Uplift and denudation of the Central Alaska Range; a case study in the use of apatite fission track thermochronology to determine absolute uplift parameters. J Geophys Res 100:20,175–20,191
Forsythe R, Nelson EP (1985) Geological manifestations of ridge collision: evidence from the Golfo de Penas-Taitao Basin, southern Chile. Tectonics 4:477–495
Forsythe R, Nelson EP, Carr MJ, Kaeding ME, Hervé M, Mpodozis C, Soffia M, Harambour S (1986) Pliocene near-trench magmatism in southern Chile: a possible manifestation of ridge collision. Geology 14:23–27
Galbraith RF (1990) The radial plot: graphical assessment of spread in ages. Nucl Tracks 17:207–214
Galbraith RF, Laslett GM (1993) Statistical models for mixed fission track ages. Nucl Tracks 21:459–470
Gleadow AJW, Duddy IR, Green PF, Lovering JF (1986) Confined fission track lengths in apatite: a diagnostic for thermal analysis. Contrib Mineral Petrol, 94:405–415
Gonzalez E (1989) Hydrocarbon resources in the coastal zone of Chile. In: Ericksen GE, Cañas MT, Reinemund JA (eds) Geology of the Andes and its relation to hydrocarbon and mineral resources Circum-Pacific council for energy and mineral resources earth science series, 11. Houston, pp 383–404
Green PF (1988) The relationship between track shortening and fission track age reduction in apatite: combined influence of inherent stability, annealing anisotropy, length bias and system calibration. Earth Planet Sci Lett 89:335–352
Green PF, Duddy IR, Laslett GM, Hegarthy KA, Gleadow AJW, Lovering JF (1989) Thermal annealing of fission tracks in apatite: 4. Quantitative modeling techniques and extension to geological time scales. Chem Geol 79:155–182
Hallet B, Hunter L, Bogen J (1996) Rates of erosion and sediment evacuation by glaciers: A review of field data and their implications, Glob Planet Change 12:213–235
Hamza VM, Muñoz M (1996) Heat flow map of South America. Geothermics 25:599–646
Harrison TM (1981) Diffusion of ^{40}Ar in Hornblende. Contrib Mineral Petrol 78:324–331
Harrison TM, Duncan I, McDougall I (1985) Diffusion of ^{40}Ar in biotite: temperature, pressure and compositional effects. Geochim Cosmochim Acta 49:2461–2468
Hervé F (1984) Rejuvenecimiento de edades radiométricas y el sistema de fallas Liquiñe-Ofqui. Com Dep Geol Univ Chile 35:107–116
Hervé F, Araya E, Fuenzalida J, Solano A (1979) Edades radiométricas y tectónica neógena en el sector costero de Chiloé Continental, X Región. Segundo Congreso Geológico Chileno, Arica, Actas 1:F1–F18
Hervé F, Pankhurst RJ, Drake R, Beck ME, Mpodozis C (1993) Granite generation and rapid unroofing related to strike-slip faulting, Aysén, Southern Chile. Earth Planet Sci Lett 120:375–386
Hervé F, Pankhurst RJ, Drake R, Beck ME (1995) Pillow metabasalts in a mid-Tertiary extensional basin adjacent to the Liquiñe Ofqui fault zone: the Isla Magdalena area, Aysén, Chile. J South Am Sci 8:33–46
Hervé F, Pankhurst RJ, Demant A, Ramirez E (1996) Age and Al-in-hornblende geobarometry in the North Patagonian Batholith, Aysén, Chile. Third International Symposium on Andean Geodynamics (ISAG), St Malo, France, abstracts, ORSTOM, Paris, pp 17–19
Hervé F, Fanning CM, Bradshaw J, Bradshaw M, Lacassie JP (1999) Late Permian SHRIMP U-Pb detrital zircon ages constrain the age of accretion of oceanic basalt to the Gondwana margin at the Madre de Dios Archipelago, southern Chile. In: Fourth ISAG, Göttingen, Germany, abstracts, ORSTOM, Paris, pp 327–328
Hervé F, Demant A, Ramos V, Pankhurst RJ, Suárez M (2000) The Southern Andes. In: Cordani UG, Milani EJ, Thomaz Filho A, Campos DA (eds) Tectonic evolution of South America. pp 605–634
Hervé F, Fanning CM (2001) Late Triassic detrital zircons in metaturbidites of the Chonos Metamorphic Complex, southern Chile. Rev Geol Chile 28(1):91–104

Hervé M (1976) Estudio Geológico de la Falla Liquiñe-Reloncaví en el área de Liquiñe: antecedentes de un movimiento transcurrente. Primer Congreso Geológico Chileno, Santiago, Actas 1:B39–B56
Heusser CJ (1990) Chilotan piedmont glacier in the Southern Andes during the glacial maximum. Rev Geol Chile 15(1):13–30
Holdaway MJ (1971) Stability of Andalusite and the aluminosilicate phase diagrams. Am J Sci 271:97–131
Hurford AJ (1986) Cooling and uplift patterns in the Lepontine Alps South Central Switzerland and age of vertical movement on the Insubric fault line. Contrib Mineral Petrol 92:413–427
Hurford AJ (1990) Standardization of fission track dating calibration: recommendation by the Fission Track Working Group of the I.U.G.S. Subcommission on Geochronology. Chem Geol 80:171–178
Hurford AJ, Green PF (1983) The zeta age calibration of fission track dating. Chem Geol 1:285–317
Hurford AJ, Hunziker JC, Stöckhert B (1991) Constraints on the thermotectonic evolution of the Western Alps: evidence for episodic rapid uplift. Tectonics 10:758–769
Hutton DHW, Reavy RJ (1992) Strike-slip tectonics and granite petrogenesis. Tectonics 11:960–967
Johnson C, Harbury N, Hurford AJ (1997) The role of extension in the miocene denudation of the Nevado-Filábride complex, Betic Cordillera (SE Spain). Tectonics 16:189–204
Kasuya M, Naeser CW (1988) The effect of α–damage on fission-track annealing in zircon. Nucl Tracks Radiat Meas 14:477–480
Ketcham RA, Donelick RA, Donelick MB (2000) AFTSolve: a program for multi-kinetic modeling of apatite fission-track data. Geol Mat Res 2(1):1–32
Kukowski N (1992) Plutonische hydrothermale Systeme in der kontinentalen Kruste: Numerische Modellrechungen zu räumlichen Dimensionen und zeitlichen Variationen von Quelle und Umfeld. PhD Thesis, University of Bonn, p 119
Kukowski N, Neugebauer HJ (1990) On the ascent and emplacement of granitoid magma bodies - dynamic-thermal numerical models. Geol Rundschau 79:227–239
Laslett GM, Kendall WS, Gleadow AJW, Duddy IR (1982) Bias in measurement of fission track length distributions. Nucl Tracks 6:79–85
Laslett GM, Green PF, Duddy IR, Gleadow AJW (1987) Thermal annealing of fission tracks in apatite: 2. A quantitative analysis. Chem Geol 65:1–13
Lavenu A, Cembrano J (1999) Compressional- and transpressional-stress for Pliocene and Quaternary brittle deformation in forearc and intra-arc zones (Andes of Central and Southern Chile). J Struct Geol 2:1669–1691
Lister GS, Snoke AW (1984) S-C Mylonites. J Struct Geol 6:617–638
Lliboutry L (1999) Glaciers of the Wet Andes. In: Williams RS, Ferrigno JG (eds) Satellite image atlas of the glaciers of the World, South America. United States Geol Survey professional paper 1386-I, http://pubs.usgs.gov.prof/p1386i/index.html
Mancktelow NZ, Grasemann B (1997) Time-dependent effects of heat advection and topography in cooling histories during erosion. Tectonophysics 270:167–195
Marsh BD (2000) Magma Chambers. In: Sigurdsson H, Houghton B, McNutt SR, Rymer H, Stix J (eds) Encyclopedia of Volcanoes. Academic, San Diego, CA, pp 191–206
Martin MW, Kato CT, Rodriguez C, Godoy E, Duhart P, McDonough M, Campos A (1999) Evolution of the Late Paleozoic accretionary complex and overlying forearc-magmatic arc, south-central Chile (38°- 41°S), Constraints for the tectonic setting along the southwestern margin of Gondwana. Tectonics 18/4:582–605
Mercer JH, Sutter JF (1982) Late Miocene-earliest Pliocene glaciation in southern Argentina: implications for global ice-sheet history. Paleogeogr Paleoclimatol Paleoecol, 38:185–206
Montgomery DR, Balco G, Willet SD (2001) Climate, tectonics, and the morphology of the Andes. Geology 29:579–582
Montgomery DR, Brandon MT (2002) Topographic controls on erosion rates in tectonically active mountain ranges. Earth Planet Sci Lett 1:481–489
Munizaga F, Hervé F, Drake R, Pankhurst RJ, Brook M, Snelling N (1988) Geochronology of the Lake Region of South Central Chile (39°- 42°S): preliminary results. J South Am Earth Sci 1(3):309–318
Muñoz M (1999) Tectonophysics of the Andes region: relationships with heat flow and the thermal structure. Fourth ISAG, Göttingen, Germany, abstracts. ORSTOM, Paris, pp 532–534
Muñoz J, Troncoso R, Duhart P, Crignola P, Farmer L, Stern C (2000) The relation of the mid-Tertiary coastal magmatic belt in south-central Chile to the late Oligocene increase in plate convergence rate. Rev Geol Chile, 27/2:177–203
Murdie RE, Prior DJ, Styles P, Flint SS, Pearce RG, Agar SM (1993) Seismic responses to ridge transform subduction: Chile Triple Junction. Geology 21:1095–1098
Naeser CW (1976) Fission track dating. US Geological Survey Open File Report, vol. 76–190
Nelson E, Forsythe R, Arit I (1994) Ridge Collision tectonics in terrane development. J South Am Earth Sci 7:271–278
New M, Lister D, Hulme M, Makin I (2002) A high-resolution data set of surface climate over global land areas. Clim Res 21:1–25
Pankhurst RJ, Hervé F, Rojas FL, Cembrano J (1992) Magmatism and tectonics in continental Chiloé, Chile (42°- 42°30'S). Tectonophysics 205:673–694
Pankhurst RJ, Leat PT, Sruoga P, Rapela CW, Márquez M, Storey BC, Riley TR (1998) The Chon-Aike silicic igneous province of Patagonia and related rocks in West Antarctica: a silicic LIP. J Volcano Geotherm Res 81:113–136
Pankhurst RJ, Weaver SD, Hervé F, Larrondo P (1999) Mesozoic-Cenozoic evolution of the North Patagonian Batholith in Aysén, southern Chile. J Geol Soc London 156:673–694
Parada M, Godoy E, Hervé F, Thiele R (1987) Miocene calcalkaline plutonism in the Chilean Southern Andes. Rev Bras Geosciências 17(4):450–455
Pardo-Casas F, Molnar P (1987) Relative motion of the Nazca (Farallon) and South American plates since Late Cretaceous times. Tectonics 6:233–248
Paterson SR, Vernon RH, Fowler Jr TK (1991) Aureole tectonics. In: Kerick D (ed) Contact Metamorphism. Rev Mineral 26:673–722
Purdy JW, Jäger E (1976) K-Ar ages on rock-forming minerals from the Central Alps. Mem Inst Geol Mineral Univ Padova 30:1–34
Rabassa J, Clapperton CM (1990) Quaternary glaciations of the southern Andes. Quat Sci Rev 9:153–174
Rahn MK, Brandon MT, Batt GE, Garver JI (2004) A zero model for fission-track annealing in zircon. Am Mineral 89:473–484
Ramos V (1989) Andean foothills structures in Northern Magallanes basin, Argentina. AAPG Bull 73:887–903
Ramos V, Kay S (1992) Southern Patagonian plateau basalts and deformation: Backarc testimony of ridge collisions. Tectonophysics 205:261–282
Rojas C, Beck ME, Burmester RF, Cembrano J, Hervé F (1994) Paleomagnetism of the mid-Tertiary Ayacara Formation, southern Chile: Counterclockwise rotation in a dextral shear zone. J South Am Earth Sci 7:45–56
Seifert W, Rosenau M, Echtler H (2003) The evolution of the South Central Chile magmatic arcs: crystallization depths of granitoids estimated by hornblende geothermobarometry – implications for mass transfer processes along the active continental margin. N Jb Geol Paläont 236:115–127
Seipold U (1998) Temperature dependence of thermal transport properties of crystalline rocks - A general law. Tectonophysics 291:161–171
Sernageomin (1980) Mapa geológico de Chile, escala 1:1.000.000. Servicio Nacional de Geología y Minería, Santiago, Chile
Sernageomin-BRGM (1995) Carta Metalogénica X Región Sur, Chile. Servicio Nacional de Geología y Minería-Bureau de Recherches Géologiques et Minières, Informe Registrado IR-95-05, 10 Vols, Santiago
Singer B, Ackert RP, Guillou H (2004) 40Ar/39Ar and K/Ar chronology of Pleistocene glaciations in Patagonia. Geol Soc Am Bull 116/3: 434–450 DOI:10.1130/B25177.1

Small E (1999) Does global cooling reduce relief? Nature 401:31–33
Somoza R (1998) Updated Nazca (Farallon)-South America relative motions during the last 40 Ma: Implications for mountain building in the central Andean region. J South Am Sci 11:211–215
Spear FS, Cheney JT (1989) A petrogenetic grid for pelitic schists in the system SiO_2-Al_2O_3-FeO-MgO-K_2O-H_2O. Contrib Mineral Petrol 83:348–357
Stöckhert B, Brix MR, Kleinschrodt R, Hurford AJ, Wirth R (1999) Thermochronometry and microstructures of quartz - a comparison with experimental flow laws and predictions on the temperature of the brittle-plastic transition. J Struct Geol 21:351–369
Stüwe K, White L, Brown R (1994) The influence of eroding topography on steady-state isotherms. Application to fission-track analysis. Earth Planet Sci Lett 124:63–74
Suarez M, De la Cruz R (2000) Tectonics in the eastern central Patagonian Cordillera (45°30'- 47°30'S). J Geol Soc London 157:995–1001
Tagami T., Shimada C. (1996). Natural long-term annealing of the zircon fission-track system around a granitic pluton. J Geophys Res 101:8245–8255
Thiele R, Hervé F, Parada MA, Godoy E (1986) The Liquiñe-Ofqui megafault at the Reloncaví Fiord (41°30'S), Chile. Comunicaciones Dep Geol Univ Chile 46:3–15
Tchalenko JS (1970) Similarities between shear zones of different magnitudes. Geol Soc Am Bull 81:1625–1640
Thomson SN (2002) Late Cenozoic geomorphic and tectonic evolution of the Patagonian Andes between latitudes 42°S and 46°S: an appraisal based on fission track results from the transpressional intra-arc Liquiñe-Ofqui fault zone. Geol Soc Am Bull 114(9):1159–1173
Thomson SN, Hervé F, Stöckhert B (2001) The Mesozoic-Cenozoic denudation history of the Patagonian Andes (southern Chile) and its correlation to different subduction processes. Tectonics 20:693–711
Tikoff B, Saint-Blanquat M (1997) Transpressional shearing and strike-slip partitioning in the Late Cretaceous Sierra Nevada magmatic arc, California. Tectonics 16:442–459
Vietor T, Echtler H (2005) Episodic Neogene southward growth of the Andean subduction orogen between 30°S and 40°S - plate motions, mantle flow, climate, and upper-plate structure. Earth Planet Sci Lett (in press)
Wagner GA, Reimer GM (1972) Fission track tectonics: the tectonic interpretation of fission track apatite ages. Earth Planet Sci Lett 14:263–268
Wagner GA, Hejl E, Van den Haute P (1994) The KTB fission-track project: methodological aspects and geological implications. Radiat Meas 23:95–101
Whipple K, Kerby E, Brocklehurst SH (1999) Geomorphic limits to climate-induced increases in topographic relief. Nature 401:39–43
Willet SD (1999) Orogeny and Orography: The effects of erosion on the structure of mountain belts. J Geophys Res, 104: 28,957–28,981